https://doi.org/10.5194/gmd-2020-34
Preprint. Discussion started: 26 February 2020

Geoscientific Model Development Discussions

Global aerosol simulations using NICAM.16 on a 14-km grid spacing for a climate study: Improved and remaining issues relative to a lower-resolution model

Daisuke Goto[1], Yousuke Sato[2,3], Hisashi Yashiro[1,3], Kentaroh Suzuki[4], Eiji Oikawa[5], Rei Kudo[6], Takashi M. Nagao[4], Teruyuki Nakajima[7]

[1]National Institute for Environmental Studies, Tsukuba, Japan

[2]Faculty of Science, Department of Earth and Planetary Sciences, Hokkaido University, Sapporo, Japan

[3]RIKEN Center for Computational Research, Kobe, Japan

[4]Atmosphere and Ocean Research Institute, University of Tokyo, Kashiwa, Japan

[5]Research Institute for Applied Mechanics, Kyushu University, Kasuga, Japan

[6]Meteorological Research Institute, Tsukuba, Japan

[7]Earth Observation Research Center, Japan Aerospace Exploration Agency, Tsukuba, Japan

Correspondence to: Daisuke Goto (goto.daisuke@nies.go.jp)

https://doi.org/10.5194/gmd-2020-34
Preprint. Discussion started: 26 February 2020

Geoscientific Model Development Discussions

Abstract. High-performance computing resources allow us to conduct numerical simulations with a horizontal grid spacing that is sufficiently high to resolve cloud systems on a global scale, and high-resolution models (HRMs) generally provide better simulation performances than low-resolution models (LRMs). In this study, we execute a next-generation model that is capable of simulating global aerosols on a nonhydrostatic icosahedral atmospheric model version 16 (NICAM.16). The simulated aerosol distributions are obtained for 3 years with a HRM in a global 14-km grid spacing, an unprecedentedly high horizontal resolution and long integration period. For comparison, a NICAM with a 56-km grid spacing is also run as an LRM, although this horizontal resolution is still high among current global climate models. The comparison elucidated that the differences in the various variables of meteorological fields, including the wind speed, precipitation, clouds, radiation fluxes and total aerosols, are generally within 10% of their annual averages, but most of the variables related to aerosols simulated by the HRM are slightly closer to the observations than are those simulated by the LRM. Upon investigating the aerosol components, the differences in the water-insoluble black carbon (WIBC) and sulfate concentrations between the HRM and LRM are large (up to 32%), even in the annual averages. This finding is attributed to the differences in the column burden of the aerosol wet deposition, which is determined by a conversion rate of precipitation to cloud and the difference between the HRM and LRM is approximately 20%. Additionally, the differences in the simulated aerosol concentrations at polluted sites during polluted months between the HRM and LRM are estimated with medians of -23% (-63% to -2.5%) for BC, -4% (-91% to +18%) for sulfate and -1% (-49% to +223%) for the aerosol optical thickness (AOT). These findings indicate that the differences in the secondary and tertiary products, such as the AOT, between the different horizontal grid spacings are not explained simply by the grid size. On a global scale, the subgrid variabilities in the simulated AOT and COT in the 1°×1° domain using 6-hourly data are estimated to be 28.5% and 80.0%, respectively, in the HRM, whereas the corresponding differences are 16.6% and 22.9% in the LRM. Over the Arctic, both the HRM and the LRM generally reproduce the observed aerosols, but the largest difference in the surface BC mass concentrations between the HRM and LRM reaches 30% in spring (the HRM-simulated results are closer to the observations). The vertical distributions of the HRM- and LRM-simulated aerosols are generally close to the measurements, but the differences between the HRM and LRM results are large above a height of approximately 3 km, mainly due to differences in the wet deposition of the aerosols. The global annual averages of the direct and indirect aerosol radiative forcings (ARFs) attributed to anthropogenic aerosols in the HRM are estimated to be -0.29 Wm^{-2} and -0.93 Wm^{-2},

https://doi.org/10.5194/gmd-2020-34
Preprint. Discussion started: 26 February 2020

Geoscientific Model Development Discussions

respectively, whereas those in the LRM are -0.24 Wm^{-2} and -1.10 Wm^{-2}. The differences in the direct ARF between the HRM and LRM are primarily caused by those in the aerosol burden, whereas the differences in the indirect ARF are primarily caused by those in the cloud expression and performance, which are attributed to the grid spacing. Because one-tenth of the computer resources are required for the LRM (56-km grid) compared to the HRM (14-km grid), we recommend that the various tuning parameters associated with the aerosol distributions using the LRM can be applicable to those using the HRM under the limitation of the available computational resources or before the HRM integration.

1 Introduction

High-performance computing resources allow us to conduct numerical simulations with a horizontal grid spacing that is sufficient fine to resolve cloud systems on a global scale. Suzuki et al. (2008) first performed a high-resolution global simulation while explicitly treating the aerosol-cloud interaction (ACI) and reproduced the interactions obtained from satellite measurements. For the past 10 years, various high-resolution models (HRMs) have been developed to address the heretofore unresolved mechanisms related to cloud processes; one example of a related outcome is the buffered system hypothesis (e.g., Stevens and Feingold, 2009; Malavelle et al., 2017). When modeling atmospheric pollutants such as aerosols and short-lived gases, HRMs are believed to provide a better simulation performance than low-resolution models (LRMs). For example, Qian et al. (2010) showed that simulations of the trace gases and aerosols in the vicinity of Mexico City in March with a 3-km horizontal resolution are far more advantageous than simulations with 15-km and 75-km horizontal resolutions; this indicates that a high-resolution horizontal grid can resolve local emissions and terrain-induced flows along mountain ridges. Similarly, Ma et al. (2014) identified that the aerosols and clouds simulated over the Arctic in April at the finest resolution (10 km) are closer to the observations than those simulated at a coarser resolution (ranging from 20 km to 160 km). In addition, using a global model with a horizontal resolution varying from 3.5 km to 56 km, Sato et al. (2016) showed that fine-resolution grids can more realistically resolve low-pressure systems with vortexes at mid-latitudes, which result in the realistic transport of black carbon (BC) to the Arctic in November, than can coarse-resolution grids. On a global scale, Sekiya et al. (2018) employed a global chemical transport model with an integration period of 1 year and provided a more realistic distribution of short-lived gaseous NO_2, especially in urban areas, with a horizontal resolution of approximately 60 km (0.56°×0.56°) than with horizontal

https://doi.org/10.5194/gmd-2020-34
Preprint. Discussion started: 26 February 2020

resolutions of approximately 110 km and 300 km (1.1°×1.1° and 2.8°×2.8°). Furthermore, Schutgens et al. (2016) investigated the subgrid variability of simulated aerosols with a 10-km resolution in various domains and noted the importance of a fine grid sizes, and Goto et al. (2016) showed that 10-km grid simulations around Japan over an integration period of 3 years require a regional HRM to properly reproduce the concentrations of aerosols since such high concentrations in urban areas create health concerns for many people (Ezzati et al., 2002). The studies mentioned above focused on atmospheric pollutants and discussed the advantages of HRMs at various scales and among different seasons; nevertheless, with only a few exceptions, their models were not executed with horizontal grids finer than 50 km for adequately long periods on a global scale. For instance, Hu et al. (2018) successfully applied the Goddard Earth Observing System (GEOS)-Chem model with a 12.5-km horizontal grid to simulate aerosols and short-lived gases, and Sato et al. (2018) clarified the advantages of a HRM using a nonhydrostatic icosahedral atmospheric model (NICAM) with a 14-km horizontal grid to resolve ACIs. However, these two studies focused on study periods of just 1 year. The 1-year calculation cannot provide the yearly variability; thus, clarifying whether the differences in the simulated results between the HRM and LRM are caused by a difference in horizontal resolution or meteorological fluctuations among years is difficult. As such, the merits of using HRMs with horizontal grid resolutions finer than 50 km to simulate aerosols in global and climatological fields remain ambiguous. Thus, it is very important to clarify this issue and to provide scientific evidence for our future; to achieve this goal, global calculations of air pollutants must be performed with HRMs in horizontal grids finer than 10 km.

Therefore, in this study, we investigate how much relatively high-resolution grids can improve the simulation results of aerosols and their interactions with clouds and radiation fluxes for climatological fields. For this purpose, we executed a NICAM with aerosol components on a 14-km horizontal grid for 3 years. This 14-km horizontal grid boasts the finest resolution among all global chemistry models and is generally finer than most regional chemistry models (Galmarini et al., 2018). To effectively show the advantages in the simulated parameters related to aerosols in the HRM with a 14-km horizontal grid, we also executed an LRM with a 56-km horizontal grid, which is still finer than most global aerosol models (Myhre et al., 2013; Galmarini et al., 2018). Some issues are still under debate in global aerosol models. For example, how well are atmospheric pollutants over the Arctic reproduced (e.g., Shindell et al., 2008)? In addition, why do most global models overestimate BC (and possibly other species) in the middle and high troposphere over the remote ocean (e.g., Schwarz et al., 2013)? Finally, what are the aerosol

https://doi.org/10.5194/gmd-2020-34
Preprint. Discussion started: 26 February 2020


Geoscientific Model Development Discussions

radiative forcing (ARF) values estimated through aerosol-radiation interactions (ARIs) and ACIs using global cloud-system resolving models? Furthermore, it is also important to quantify the differences caused by the horizontal grid spacing or yearly variability of the meteorological fields.

In this paper, the models and observation datasets are described in section 2. Section 3 demonstrates the results of using the NICAM coupled to an aerosol module and compares the results with multiple measurements. The first part of section 3 illustrates the global distributions of meteorological fields such as winds, precipitation, clouds, and radiation, while the second part shows the results of evaluations with the HRM and LRM using multiple aerosol measurements. In section 4, the effects of different grid spacings on the aerosol fields, model evaluations over the Arctic, ARFs, uncertainties caused by the meteorological fields and required computational resources are discussed. Section 5 provides the summary of this work and the implications for future research on HRMs in the context of powerful computational resources.

2 Model descriptions and experimental design

2.1 NICAM

Aerosol simulations were performed with a nonhydrostatic icosahedral atmospheric model (NICAM) with a uniform grid system (Tomita and Satoh, 2004; Satoh et al. 2008; 2014). The NICAM was executed with unprecedentedly high resolutions, namely, 0.87 km for 1 week (Miyamoto et al., 2012) and 14 km for 25 years under Atmospheric Model Intercomparison Project (AMIP)-like experiments (Kodama et al., 2015), although these studies did not consider aerosols. Subsequently, Suzuki et al. (2008) first conducted a global 7-km integration of aerosols for 1 week in July 2006 and validated the simulated ACIs by comparing them with satellite measurements. Sato et al. (2016) performed a global 3.5-km integration of aerosols for 2 weeks in November 2011 to focus on the transport and deposition of BC over the Arctic. Jing et al. (2017) and Sato et al. (2018) analyzed cloud microphysics parameters simulated by a NICAM with aerosol components and a 14-km grid spacing for 1 year in 2012. Additionally, to analyze the transport of a simulated tracer in a HRM, Ishijima et al. (2018) calculated a radon tracer that has a long lifetime in the atmosphere using a NICAM with a 14-km horizontal resolution for 3 years. However, these studies did not elucidate the distributions of the aerosol components on a global scale for more than 1

https://doi.org/10.5194/gmd-2020-34
Preprint. Discussion started: 26 February 2020


Geoscientific Model Development Discussions

year. Therefore, the present study extends these studies by simulating aerosol components for 3 years to discuss them climatologically.

The NICAM, which corresponds to a dynamic core, simulates the basic prognostic variable such as air temperature, wind, water vapor, cloud, precipitation and radiation fluxes by calculating different processes, such as advection and diffusion, and the corresponding physics. In this study, the NICAM developed in 2016 was used as NICAM.16. The options to use modules for these calculations in running the NICAM with a 14-km resolution are almost similar to those used in Kodama et al. (2015). The advection module is based on Miura (2007) and Niwa et al. (2011), and the diffusion module is the level 2 Mellor-Yamada-Nakanishi-Niino (MYNN) scheme (Mellor and Yamada, 1972; Nakanishi and Niino, 2004). The module for calculating the land surface flux is the Minimal Advanced Treatments of Surface Interaction and Runoff (MATSIRO) model with boundary conditions such as the land cover type, soil type, leaf area index and ground albedo (Takata et al., 2003). The Model Simulation Radiation Transfer code (MSTRN-X), which is based on the k-distribution scheme, is adopted for the radiation model to calculate the radiative fluxes by considering the scattering, absorption and emissivity of aerosols and clouds and their absorption by gases (Sekiguchi and Nakajima, 2008). The MSTRN-X also calculates the global, direct and diffuse solar fluxes. The cloud microphysics module is NICAM Single-Moment Water 6 (NSW6) (Tomita, 2008), which prognoses the single-moment bulk amounts of 6 categorized hydrometeors, i.e., water vapor, cloud water, rain, cloud ice, hail and graupel. Cloud water and rain are affected by cloud condensation nuclei (CCN), which are calculated by the parameterization of Abdul-Razzak and Ghan (2000) as an indirect aerosol effect (IARF). The parameterization of aerosol activation considers the updraft velocity, aerosol sizes and aerosol chemical compositions. Even in a HRM, the updraft velocity tends to be small; therefore, the updraft velocity is also parameterized by the formulation proposed by Lohmann et al. (1999) using turbulent kinetic energy, and the minimum value of the updraft velocity is set to 0.1 ms^{-1} (Ghan et al., 1997). The minimum number of CCN is set at 25 cm^{-3}, as defined in the previous studies (Jing et al., 2017; Sato et al., 2018). Under high-resolution horizontal grid simulations, a NICAM does not generally adopt a cumulus parameterization or define the cloud fraction (e.g., Satoh et al., 2010; Goto et al., 2015a; Goto et al., 2019). This study defines a warm-cloud frequency, which is set to 1 when (1) the sum of all hydrometers except water vapor exceeds 10^{-4} kg m^{-3}, (2) the cloud liquid water content (LWC) exceeds 10^{-3} kg m^{-3} and (3) the cloud optical thickness (COT) exceeds 0.2 (Sato et al., 2018). The

https://doi.org/10.5194/gmd-2020-34
Preprint. Discussion started: 26 February 2020


Geoscientific Model Development Discussions

autoconversion rate from cloud to raindrops is parameterized by Berry (1967). The simulated relationship between cloud and precipitation with a 14-km grid spacing has already been thoroughly evaluated in previous studies (Jing et al., 2017; Sato et al., 2018).

2.2 Aerosol module

The aerosol module, based on the Spectral Radiation-Transport Model for Aerosol Species (SPRINTARS) (Takemura et al., 2005), was implemented in NICAM by Suzuki et al. (2008) and the results were sufficiently validated through previous studies on a global scale with low-resolution (approximately 200 km) horizontal grids (Dai et al., 2014; Dai et al., 2018; Goto et al., 2015b) and on the regional scale with high-resolution (10-25 km) horizontal grids (Goto et al., 2015a; Goto et al., 2016; Goto et al., 2019); moreover, the results were validated on a global scale with horizontal grids at high resolutions (ranging from 3.5 km to 14 km) but over a relatively short period of less than 1 month (Suzuki et al., 2008; Sato et al., 2016; Goto et al., 2017). The use and applications of this module are summarized in Goto et al. (2018). The aerosol module considers major tropospheric aerosol species, i.e., BC, particulate organic matter (POM), sulfate, dust and sea salt. BC is a primary particle that is emitted from anthropogenic sources and biomass burning. One-half of all BC particles emitted from anthropogenic sources are assumed to be hydrophobic, whereas the remainder are assumed to be hydrophilic as internally mixed particles with POM without any atmospheric aging (Takemura et al., 2005). These emitted aerosols are transported, diffused and removed through wet deposition in and below clouds by precipitation, dry deposition and gravitational settling, which are described elsewhere in the literature (e.g., Goto et al., 2015a; Goto et al., 2019). Especially, for the wet deposition of aerosols, the previous versions of the global climate model with a coarse resolution were updated to adapt to various assumptions to produce simulations with a finer resolution (Goto et al., 2019). The secondary aerosol sulfate (the main secondary aerosol considered in this study) is formed from chemical reactions, namely, the oxidation of SO_2 by OH, ozone and H_2O_2 in the atmosphere. The three-dimensional distribution of these oxidants is prescribed from the results of a chemical transport model, namely, the chemical atmospheric general circulation model (AGCM) for study of atmospheric environment and radiative forcing (CHASER), coupled to a conventional GCM named the Model for Interdisciplinary Research on Climate (MIROC) (Sudo et al., 2002). The sizes of dust and sea salt are divided into 10 bins (the centers are

https://doi.org/10.5194/gmd-2020-34
Preprint. Discussion started: 26 February 2020


Geoscientific Model Development Discussions

from 0.13 μm to 8.02 μm) and 4 bins (the centers are from 0.178 μm to 5.62μm), respectively, whereas those of BC, POM and sulfate are assumed to be one modal with constant sizes (the radii are 0.1 μm for internally mixed BC with POM, 0.08 μm for SOA and 0.054 μm for external BC). For internally mixed BC with POM, SOA, sulfate and sea salt, i.e., hygroscopic particles, the sizes are functions of the relative humidity (RH) (e.g., Table 2 in Goto et al., 2011). For all aerosols, their optical products, i.e., their extinction coefficient and AOT, are calculated by their mass concentrations and properties such as size, RH and refractive index according to Mie scattering (Sekiguchi and Nakajima, 2008). These optical parameters at a wavelength of 550 nm are evaluated by measurements. The refractive indexes are 1.53-0.0055i for dust, 1.50-10^{-8}i for sea salt, 1.43-10^{-8}i for sulfate, 1.53-0.006i for pure POM and 1.75-0.44i for pure BC (Dai et al., 2014). The refractive indexes for internally mixed BC with POM are calculated by the volume-weight average. To evaluate the aerosol direct effect in the NICAM, the flux of the ARI is calculated by the difference in the radiative fluxes with/without aerosol species in MSTRN-X; the ARI due to anthropogenic aerosols is also calculated by the difference in the radiative fluxes between two different experiments with/without anthropogenic aerosol species (but the emissions from biomass burning do not change in our assumption). In these two experiments with/without anthropogenic sources, the forcing of the ACI due to anthropogenic aerosols is also calculated by the difference in the cloud radiative fluxes; the method for calculating the ACI as an effective ARF is derived from Ghan (2013). Unfortunately, the calculations of the ACI under the pre-industrial era and the ARI associated with each aerosol component under the present era are only performed for one year because of limitations of available computer resources. Therefore, the ACI value and the ARI value associated with each aerosol component are calculated using the one year integration

2.3 Experimental design

Numerical experiments with the HRM (14-km horizontal grid) are carried out for 3 years, and experiments are also carried out with the LRM (56-km horizontal grid) for the same period. In both the HRM and the LRM, the number of vertical layers is set at 38, which is relatively small but was still used in previous studies (Kodama et al., 2015; Sato et al., 2016; Sato et al., 2018). The heights of the layers are 80.8 m at the bottom to 36.7 km at the top of the model domain; 10 layers are used below a height of approximately 2 km. The timestep is set at 1 minute in both the HRM and the LRM, and the initial

https://doi.org/10.5194/gmd-2020-34
Preprint. Discussion started: 26 February 2020


Geoscientific Model Development Discussions

conditions are prepared by the meteorological fields estimated from the National Centers for Environmental Prediction (NCEP)-Final (FNL) (Kalnay et al, 1996) data on November 2011 for the model spinup. The analysis is initiated at the beginning of January 2012 and terminates in December 2014. The model runs without nudging the meteorological fields, i.e., in a free run. The sea surface temperature (SST) and sea ice are nudged by the results of the NICAM from Kodama et al. (2015).

The emission amounts of total BC were 5.6 Tg yr^{-1} from anthropogenic sources in 2010 according to the Hemispheric Transport of Air Pollution (HTAP)-v2.2 emission inventory (Janssen-Maenhout et al., 2015) and an average of 1.8 Tg yr^{-1} from biomass burning over 2005-2014 from the Global Fire Emission Database version 4 (GFEDv4; van der Werf et al., 2017). The injection height is set at the surface for anthropogenic sources and 1-km height for biomass burning in this study. POM is composed of both primary and secondary components; the emission amounts of primary POM were 20.3 Tg yr^{-1} for anthropogenic sources (HTAP-v2.2) and 39.7 Tg yr^{-1} from biomass burning (GFEDv4). These POM values are converted by multiplying the corresponding values for particulate organic aerosols by 1.6 for anthropogenic sources and 2.6 for biomass burning sources (Tsigaridis et al., 2014). Secondary organic aerosols (SOAs) are assumed to be particles by multiplying the emission fluxes of isoprene and terpenes provided by the Global Emissions Initiative (GEIA) (Guenther et al., 1990) using scaling factors. As a result, the amount of emitted SOAs was 22.2 Tg yr^{-1}, which is comparable to the best estimates from recent studies (Tsigaridis et al., 2014). Sulfate is a secondary species formed from a precursor of SO_2, of which 108.1 Tg yr^{-1} is emitted from anthropogenic sources (HTAP-v2.2), 2.2 Tg yr^{-1} is emitted from biomass burning (GFEDv4), and 3.1 Tg yr^{-1} is emitted from volcanic eruptions (Diehl et al., 2012). Some SO_2 is formed from dimethyl sulfide (DMS), which is emitted mainly from oceans and is calculated as a function of downward solar fluxes (Bates et al., 1987) and is estimated to be 26.2 Tg yr^{-1} (HRM) and 24.9 Tg yr^{-1} (LRM) in this study. Dust and sea salt are primary particles, which are calculated inside the model using the wind speed at a height of 10 m. The emission flux of dust depends on the cube of the wind speed as well as on the land use and snow cover (Takemura et al., 2000). Over the sea surface without sea ice, the emission flux of sea salt depends on a power of 3.41 (Monahan et al., 1986), which is comparable to the best estimate of 3.5 (Grythe et al., 2014). The estimated emission fluxes for dust and sea salt are shown in section 3.

https://doi.org/10.5194/gmd-2020-34
Preprint. Discussion started: 26 February 2020

2.4 Data description

Table 1 summarizes the measurements used in this study for the model evaluation. Satellite observations greatly assist in better understanding the global model performance of optical properties. The Moderate Resolution Imaging Spectroradiometer (MODIS), a sensor on board the polar-orbiting satellite Terra, observes both aerosols and clouds. The cloud products, i.e., COT and cloud fraction (CF), and the aerosol products, i.e., AOT, in collection 6 are retrieved by a NASA algorithm (Platnick et al., 2015). In addition, the vertical profiles of the aerosol extinction coefficients are derived from Cloud-Aerosol Lidar with Orthogonal Polarization CALIOP/Cloud-Aerosol Lidar and Infrared Pathfinder Satellite Observations (CALIPSO) version 3 provided by the NASA Langley Research Center (LaRC) after an averaging operation with a grid of 1°×1° under clear-sky conditions (Winker et al., 2013). The top-of-atmosphere (TOA) radiation fluxes, i.e., outgoing shortwave radiation (OSR), outgoing longwave radiation (OLR) and shortwave and longwave cloud radiative forcing (CRF), prepared by a CERES_EBAF_Ed2.8 level-3 product are obtained from a sensor of the Clouds and the Earth's Radiant Energy System (CERES) experiment onboard Terra and Aqua in 1°×1° grids (Loeb et al., 2009). The Baseline Surface Radiation Network (BSRN) observes surface radiation fluxes at sites worldwide (Ohmura et al., 1998). The data collected by the BSRN cover the period of 2008-2012; these data are climatologically averaged while considering missing data and are then converted to the selected 25 sites (global radiation) and 20 sites (direct and diffuse radiations) in this study. The reanalyzed wind at a height of 10 m, which is important for analyzing the emissions of dust and sea salt in the NICAM, is prepared in a product with a grid of 2.5°×2.5° by the NCEP/National Center for Atmospheric Research (NCAR) reanalysis 1 (Kalnay et al., 1996). Precipitation, which directly causes the wet removal of aerosols, is compared with a product provided by the reanalysis data of the Global Precipitation Climatology Project (GPCP) (Adler et al., 2003). The abovementioned measurements can provide a global map of the horizontal distributions of these parameters, whereas the following measurements are performed at ground-based sites spread around the world (Figure 1). The Aerosol Robotic Network (AERONET) (Holben et al., 1998) and SKYNET radiometer network (Nakajima et al., 1996) observe the AOT at sites worldwide, but only 135 AERONET sites and 5 SKYNET sites are used in this study. For the selection of these data, monthly mean values are calculated by using more than 90 samples in one month, and the annual mean values are averaged by using more than 7 months of data at each site. The China Aerosol Remote Sensing Network (CARSNET) also observes

https://doi.org/10.5194/gmd-2020-34
Preprint. Discussion started: 26 February 2020


Geoscientific Model Development Discussions

the AOT at 50 sites in China (Che et al., 2015) and directly provides climatological values for the period of 2002-2013. The AOT and extinction values are calculated at the wavelength of 550 nm in NICAM, whereas these values are retrieved at the wavelengths of 550 nm in MODIS, 500 nm AERONET and 532 nm in CALIOP. This study ignores the differences in the AOT values among the wavelengths of 500 nm, 532 nm and 550 nm because the magnitude is small (less than several percent). In addition, we compared the simulated AOT and aerosol extinction coefficient under the all-sky conditions with the satellite-retrieved AOT and coefficients under the clear-sky conditions, because the differences in the simulated AOT between all-sky and clear-sky conditions are within 10% at a global scale and at most 20% at a regional scale (Dai et al., 2015). The difference would be generally lower than that between the NICAM and satellite results. Aerosol mass concentrations are observed by multiple networks, namely, the Interagency Monitoring of Protected Visual Environments (IMPROVE) program, European Monitoring and Evaluation Programme (EMEP), Acid Deposition Monitoring Network in East Asia (EANET), China Meteorological Administration Atmosphere Watch Network (CAWNET) and University of Miami network. The IMPROVE-observed BC, POM and sulfate over North America are used at approximately 190 sites, whereas the EMEP-observed BC, POM and sulfate over Europe are employed at approximately 50 sites. Over Asia, the EANET-observed sulfate is used at only 35 sites, whereas the CAWNET-observed BC, POM and sulfate are used at 14 sites, but only in China (Zhang et al., 2012). The network managed by a group at the University of Miami releases both dust and sea salt mass concentrations at sites worldwide (e.g., Prospero et al., 1989), but only the 16 sites shown in Liu et al. (2007) are used in this study. BC measurements, especially over the Arctic, are obtained by applying an aethalometer or a particle soot absorption photometer (PSAP), which may include some biases (Sinha et al., 2017; Sharma et al., 2017); nevertheless, these measurements can still be a good reference for the evaluation of global models. Aircraft measurements of BC using a single-particle soot photometer (SP2; Schwarz et al., 2006) are also used for a 1-year model evaluation (January, March, June, August and November) in 2009 over the Pacific Ocean under the High-performance Instrumented Airborne Platform for Environmental Research (HIAPER) Pole-to-Pole Observations (HIPPO) campaign (Schwarz et al., 2010; Wofsy et al., 2012), in March-April 2012 under the Aerosol Radiative Forcing in East Asia (A-FORCE) campaign (Oshima et al., 2012), and in April-May and July-August 2008 under the Arctic Research of the Composition of the Troposphere from Aircraft and

https://doi.org/10.5194/gmd-2020-34
Preprint. Discussion started: 26 February 2020


Geoscientific Model Development Discussions

Satellites (ARCTAS) campaign (Jacob et al., 2010). The uncertainties in the observed products used in this study are shown in each reference.

3 Results

First, the meteorological fields relevant to the aerosol distribution are compared between the satellite and reanalysis data. Aerosols are transported in the atmosphere by wind and are removed from the atmosphere mainly by wet deposition associated with cloud precipitation; however, some aerosols, i.e., dust and sea salt, are emitted through surface friction by winds. Therefore, the simulated variables of wind, precipitation and clouds are evaluated. Second, the aerosols simulated by the HRM and LRM are compared with the multiple observations described in section 2.4. When measurements are not available in the model evaluation, only the difference between the HRM and LRM is discussed.

3.1 Meteorological fields

Figure 2 illustrates the annual, January and July averages of the wind directions and speeds at a 10-m height using the HRM-simulated, LRM-simulated and NCEP-reanalyzed winds. The global annual averages of both the HRM-simulated and the LRM-simulated wind speeds are higher than those of the NCEP-reanalyzed wind speeds by at most 10%. The spatial patterns of the HRM-simulated and LRM-simulated winds are generally in agreement with those obtained from the NCEP-reanalysis data, but there are slight differences between the models and the NCEP-reanalysis data and between the HRM and LRM simulations. The former (the difference between the models and reanalysis data) is predominantly caused by an underestimation over the Southern Ocean (within 45°S-90°S) and is partly attributable to an overestimation over the western Pacific, the northern Indian Ocean and the eastern Pacific in the vicinity of Mexico. In January and July, the global averages of both the HRM-simulated and the LRM-simulated wind speeds are lower than those of the NCEP-reanalyzed wind speeds by at most 10%. In January, the HRM-simulated wind speeds are slightly lower than the NCEP-reanalyzed wind speeds but higher than the LRM-simulated wind speeds, especially over the Southern Ocean, whereas in July, the HRM-simulated wind speeds are lower than the NCEP-reanalyzed and LRM-simulated wind speeds, especially over the western Pacific and the northern Indian Ocean. Although we expected the HRM-simulated wind speeds to be higher than the LRM-simulated wind

https://doi.org/10.5194/gmd-2020-34
Preprint. Discussion started: 26 February 2020


Geoscientific Model Development Discussions

speeds, our results do not confirm this behavior because the wind speed can be influenced by several complex mechanisms, such as clouds and radiation.

The precipitation simulated with the NICAM (both the HRM and the LRM) is generally comparable to the GPCP-reanalyzed precipitation, especially over the mid-latitudes and high latitudes (Figure 3a). The strongest precipitation is found at Intertropical Convergence Zone (ITCZ), where the precipitation simulated by the NICAM is overestimated compared to that reanalyzed by the GPCP and the HRM-simulated precipitation is closer to the GPCP-reanalyzed precipitation compared to the LRM-simulated one. The annual global mean values of the precipitation are 2.64 mm day^{-1} (HRM-simulated), 2.81 mm day^{-1} (LRM-simulated) and 2.64 mm day^{-1} (GPCP-reanalyzed), which is primarily because the LRM occasionally provides stronger precipitation along some coastlines than does the HRM, the HRM precipitation is closer to the GPCP precipitation than that of the LRM.

The simulated clouds are also evaluated by zonal averages based on a comparison with satellite observations (MODIS) using the water-phase CF and water-phase COT in Figure 3(b) and 3(c). The global averages of the CF are 0.06 (HRM) and 0.08 (LRM), whereas the global average of the CF in MODIS is 0.28. For the COT, a similar tendency (i.e., the NICAM-simulated clouds are underestimated compared to the satellite observations) is found in Figure 3 (c), which shows global averages of 7.9 (HRM) and 10.2 (LRM), whereas the global average in MODIS is 15.1. Such discrepancy in clouds between global models, including NICAM and the observations, can be found in previous studies (e.g., Nam et al., 2012; Kodama et al, 2015); therefore, our case also includes some common problems. In terms of the zonal distribution, however, the HRM results tend to be closer to the MODIS results compared to that of the LRM over low latitudes from 30°S to 30°N. Due to the coarseness of the horizontal grid spacing, the LRM tends to reproduce unrealistically strong convective clouds compared to the HRM. Such convective clouds can lead to strong precipitation, which is why the LRM tends to reproduce stronger precipitation and larger clouds compared to the HRM.

For the aerosol wet removal, the ratio of precipitation to cloud water (RPCW) is one of the important variables, although this is not a pure ratio of both variables but the conversion ratio from cloud to precipitation. The RPCW at a 2-km height is calculated online using the model and plotted in Figure 3(d). The global average of the RPCW at a 2-km height is calculated to be 0.143 (HRM) and 0.181 (LRM), which can be explained by the tendency that the LRM reproduces stronger convective

https://doi.org/10.5194/gmd-2020-34
Preprint. Discussion started: 26 February 2020


Geoscientific Model Development Discussions

clouds and precipitation, thus providing a quicker conversion from cloud to precipitation in the LRM compared to the HRM. Therefore, the wet removal rate in the HRM is slower than that in the LRM. This result is very important for determining the aerosol distributions.

To further evaluate the climatic impacts of clouds on the radiation field in the models, the TOA shortwave radiative fluxes and CRF between the NICAM and the satellite-based results are shown in Figures 3(e) and 3(f). The relevant TOA parameters for aerosols are the OSR and shortwave CRF (SWCRF) simulated by the HRM and LRM and retrieved by CERES. As shown in Figures 3(e) and 3(f), the global averages of these variables in the LRM appear closer to those in CERES than the averages of the HRM, which is caused by the results over the mid latitudes from 60°S to 30°S or from 60°N to 30°N. Over the low latitudes from 30°S to 30°N, where both CF and COT in the HRM are close to the MODIS results shown in Figures 3(b) and 3(c), the zonal distributions of the simulated SWCRF and OSR in the HRM are much closer to the those in CERES compared with than those in the LRM. Interestingly, these shortwave radiative fluxes in both the HRM and the LRM are closer to the fluxes retrieved by CERES than those shown in the NICAM without aerosol components by Kodama et al. (2015). This finding indicates that aerosols and their interactions with clouds primarily affect low-level clouds (mainly water-phase clouds) and provide better results than previous results without aerosols. Such effects were considered in a very recent study by Kodama et al. (submitted). Although there are some differences between the NICAM and CERES, these estimates are generally within multimodel uncertainties (8 Wm^{-2} for the SWCRF and up to 11 Wm^{-2} for the LWCRF) derived from the current global climate models (Lauer and Hamilton, 2013).

To perform a precise validation of radiative fluxes, the surface shortwave radiative fluxes simulated by NICAM are evaluated using in situ observations in Figure 4, which illustrates the scatterplots of the global, direct and diffuse radiative fluxes between the observations and NICAM simulations under all-sky conditions at the ground-based BSRN sites (almost 20 sites around the world, i.e., North America, Europe, North Africa, Asia, and Oceania). The NICAM-simulated global radiations are very similar to the observations, exhibiting high Pearson correlation coefficients (PCCs) (PCC=0.89 in both the HRM and the LRM), a low normalized mean bias (NMB) in both models (NMB=1.1% in the HRM and NMB=-0.3% in the LRM) and low uncertainties signified by small root-mean-square errors (RMSEs) (RMSE=-32 Wm^{-2} in both the HRM and the LRM). When the global radiation is decomposed into direct and diffuse radiations, however, the NICAM-simulated

https://doi.org/10.5194/gmd-2020-34
Preprint. Discussion started: 26 February 2020


Geoscientific Model Development Discussions

direct radiation fluxes are overestimated compared to the observations, while the NICAM-simulated diffuse radiation fluxes are underestimated. The correlations of these decomposed radiation fluxes are still high, except for the diffuse radiation in the LRM (PCC=0.63, which is still moderate). Moreover, the biases of the decomposed radiation components are much larger than the bias of the global radiation; the NMBs in the direct radiation are 28.2% (HRM) and 26.7% (LRM), whereas those in the diffuse radiation are -18.3% (HRM) and -20.4% (LRM). The differences in the global radiation between the HRM and LRM are very small, but the HRM-simulated direct and diffuse radiations are slightly better than the LRM-simulated radiations. These results at the surface may not be consistent with the results of the clouds and TOA radiation fluxes shown in Figures 3(e) and 3(f), respectively, which is likely because the number of samples at BSRN in Figure 4 is smaller than that by the satellites in Figures 3(e) and 3(f). In addition, the BSRN sites do not cover the oceans, which cover a considerable proportion of the globe, thereby affecting the global average. Nevertheless, considering the model performance, the simulated clouds and radiation fluxes are generally acceptable for use in global aerosol simulations with a climate model.

3.2 Aerosol fields

Figure 5 shows the global distributions of the annual, January and July averages of the HRM-simulated, LRM-simulated and MODIS-retrieved AOTs. The global annual averages of the HRM-simulated AOT (0.177) and the LRM-simulated AOT (0.171) are overestimated compared to that of the MODIS-observed AOT (0.159), whereas those of the HRM-simulated and LRM-simulated AOTs over land (0.215 and 0.209) are comparable to that of the MODIS-retrieved AOT within 0.04 (approximately 20%). This means that both the HRM-simulated and the LRM-simulated AOTs over the ocean are overestimated. The same tendencies are also found in January and July. In the Southern Ocean, for example, the NICAM-simulated AOT is overestimated compared to the MODIS-retrieved AOT by at most 0.2. In July, the NICAM-simulated AOT over the Arabian Sea is much overestimated compared to the MODIS-retrieved AOT. Over land, where the MODIS-retrieved AOT is still uncertain, the NICAM-simulated AOT is overestimated in the Saharan Desert in July and underestimated in China in January. As a result, over land, both the HRM-simulated AOT and the LRM-simulated AOT are underestimated in January and overestimated in July in comparison with the MODIS observations. Figure 6 shows the global distributions of the statistical metrics, i.e., PCC, RMSE and NMB, for the annually averaged AOTs between the NICAM

https://doi.org/10.5194/gmd-2020-34
Preprint. Discussion started: 26 February 2020


Geoscientific Model Development Discussions

simulations and MODIS retrievals. The correlations between the NICAM (both the HRM and the LRM) and MODIS are moderate with a PCC of approximately 0.410 (0.410-0.413) for the global averages and PCCs ranging from 0.432 to 0.445 for the land averages. The spatial distribution of the PCC shows mostly positive values but displays negative values in some regions, such as Eastern Europe and the oceans, at high latitudes. The global annual average RMSEs between the NICAM simulations and MODIS retrievals are calculated to be 0.146 and 0.150 (HRM and LRM, respectively), which are slightly lower than the global AOT averages (0.177 and 0.171). The RMSEs are higher than those in other regions with relatively high AOTs, such as western Africa and western Asia near the Arabian Sea, in the oceans within 40°S-70°S where the NICAM-simulated sea salt seems to be overestimated, and in eastern China and central Russia where the NICAM-simulated AOT is highly underestimated compared to the MODIS-retrieved AOT. The RMSEs over land (0.213 to 0.226) are higher than those over the oceans (0.114 to 0.115), primarily because the AOTs over the oceans are lower than those over land but also because those over deserts are higher due to the presence of dust. The NMBs are calculated to be 10.3% (HRM) and 7.1% (LRM) for the global averages and +2.1% (HRM) and -1.0% (LRM) for the land averages. High positive biases are found in the same regions with relatively high RMSEs. In the regions where both the bias and the uncertainty are high, the differences in the RMSE and NMB between the HRM and LRM are small; therefore, the high bias and high uncertainty in western Africa, western Asia, and the oceans within 40°S-70°S cannot be solved by employing finer horizontal resolutions. The largest difference in the NMBs between the HRM and LRM is found in the vicinity of the western Pacific and the northern Indian Ocean, where the difference in the precipitation between the two is also large, which is partly shown in Figure 2(a). In these regions, although the AOTs and their RMSEs are lower than those in other regions, aerosols could be important because they act as a main trigger for the onset of the monsoon season (e.g., Li et al., 2016) and because sporadic biomass burning occurs throughout the dry season.

Although polar-orbiting satellites cover large areas and provide global AOT distributions, the accuracy of satellite-retrieved AOTs is lower than that retrieved from ground-based measurements. Figure 7 shows scatterplots of the AOTs between the NICAM simulations and satellite observations, including AERONET, SKYNET and CARSNET, whose site locations are shown in Figure 1. A comparison of the AOTs between the NICAM simulations and satellite retrievals shows almost no differences between the HRM and LRM, but a comparison with in-situ measurements shows differences between the HRM

https://doi.org/10.5194/gmd-2020-34
Preprint. Discussion started: 26 February 2020


Geoscientific Model Development Discussions

and LRM. The HRM-simulated AOTs have a higher correlation (PCC=0.471), lower uncertainty (RMSE=0.21), and lower bias (NMB=-20.2%) in the annual averages compared to the LRM-simulated AOTs with PCC=0.356, RMSE=0.24 and NMB=-26.6%. Furthermore, the tendencies obtained in the annual averages are similar to those obtained in the January and July averages; this is probably because the sites are located over land, including a variety of regions (not only dusty areas, which cause the overestimation of the modeled AOTs), where the HRM-simulated AOTs are closer to the MODIS results (Figures 6 and 7). More details of the differences between the HRM and LRM are discussed in section 4.1.

To further investigation of these differences in AOTs, the differences in the decomposed AOT components in the HRM and LRM are compared in Figure 8. The global annual difference in the total AOT is calculated to be -0.005, i.e., -3.3%, which is very small. For dust and sea salt, the annual and global averages are also very small (within 0.001 or approximately 1.5%). Near the regions where these aerosols are emitted from the surface, however, the differences range from -0.1 to +0.2. For carbon and sulfate, the global and annual differences in the AOT are relatively high (-5.2% for carbon and -11.3% for sulfate). Compared to the results for dust and sea salt, the differences in the AOTs between the HRM and LRM are localized. The differences in the carbonaceous AOT are shown over land, where biomass burning occurs and anthropogenic sources are emitted. When the values in the source region are positive, those in the outflow region are negative since the simulated carbonaceous aerosols are mostly POM and the most common emission inventories are used in both the HRM and the LRM. This phenomenon is remarkable in biomass burning areas such as central Africa, South America and the western Pacific. In India, the HRM-simulated carbonaceous AOT is higher than the LRM-simulated AOT. For sulfate, most regions such as China, India and the Middle East show negative values; i.e., the HRM-simulated AOTs are clearly higher than the LRM-simulated AOTs.

Since the AOT depends on not only aerosol mass loading but also RH, the mass loadings of the aerosol components are directly compared between the HRM and LRM in Figure 9. As shown in these AOT comparisons, the global and annual differences in the dust mass loadings are very small (0.32 mg m^{-2} or 0.6%), although the regional differences are not small in the outflow regions, such as the Arabian Sea. The difference in the sea salt mass loadings between the HRM and LRM is larger than that in the sea salt AOTs by more than a factor of two, which probably cancels the difference in the mass loadings by the RH difference. The difference in the sulfate mass loadings (-0.48 mg m^{-2} or -15.7%) is larger than that in the sulfate

https://doi.org/10.5194/gmd-2020-34
Preprint. Discussion started: 26 February 2020


Geoscientific Model Development Discussions

AOTs (-11.3%). The carbon components can be decomposed into POM, water-soluble BC (WSBC) and water-insoluble BC (WIBC). The global and annual averages of the differences in these mass loadings between the HRM and LRM are all negative and are calculated to be -0.20 mg m^{-2} (-9.9%) for POM, -0.01 mg m^{-2} (-10.4%) for WSBC and -0.04 mg m^{-2} (-32.1%) for WIBC. The regional differences in POM and WSBC are noticeable near the source regions, whereas those in WIBC are found to be not only near the source regions but also largely distributed even throughout the Arctic. These comparisons of aerosol mass loadings show that the differences in the components, especially WIBC, sulfate, WSBC and POM, between the HRM and LRM are remarkable.

The global budgets of these aerosols are summarized in Table 2, which includes the mass loading or column density, chemical budget (emissions and deposition through dry processes, gravitational settling and wet processes), and atmospheric lifetime. These values are generally within the variabilities and uncertainties estimated by other global models (e.g., Textor et al., 2006), except for the lifetimes of some aerosols. The lifetimes of sulfate are estimated to be 2.38 days (HRM) and 2.05 days (LRM), which are smaller than those (ranging from 3.3 days to 4.9 days) in the literature (Textor et al., 2006; Matsui and Mahowald, 2017). For sea salt, the lifetime is approximately 0.2 days (both the HRM and the LRM), which is in the lower limit of the references (0.20-0.98 days by Textor et al., 2006; Matsui and Mahowald, 2017; Bian et al., 2019). Since the lifetimes of POM and BC are within the variabilities reported among the previous studies, the wet deposition fluxes, especially over the oceans, seem to be larger, which is mainly due to the larger RPCW values shown in Figure 3(d) using cloud-system resolving models. The lifetimes of the WIBC are comparable to that in a previous study by Goto et al. (2012) but much longer than that of the previous studies that considered the atmospheric aging (Chung and Seinfeld, 2002; Goto et al., 2012). Additionally, the differences between the HRM and LRM in the wet deposition flux of sea salt and the atmospheric lifetimes of both BC and WIBC are relatively large (more than 20%), whereas the differences in the dust column and budgets are very small. Therefore, the impact of the horizontal resolution (14-km and 56-km grid spacings) on dust is very small, but sea salt, sulfate and BC are strongly influenced.

Since almost all aerosols are emitted from the surface, evaluations of the surface mass concentrations of those aerosols are important. Figure 10 shows the global distributions of the differences in the annual averages of the aerosol surface mass concentrations between the HRM and LRM. Compared to the differences in the AOTs and mass loadings, the differences in

https://doi.org/10.5194/gmd-2020-34
Preprint. Discussion started: 26 February 2020


Geoscientific Model Development Discussions

the surface mass concentrations are generally smaller but have different signs for carbonaceous aerosols, i.e., POM, WSBC and WIBC. This is probably because the NICAM-simulated biomass burning-emitted aerosols, i.e., parts of carbonaceous aerosols, are ejected to a height of 1 km (not the surface). For dust, sea salt and sulfate, the horizontal patterns of the differences in their surface mass concentrations between the HRM and LRM are similar to those in the AOTs and mass loadings. The simulated surface mass concentrations are evaluated by the measurements described in section 2.4, and the results are shown in Figures 11 and 12, which illustrate scatterplots of the annually averaged surface mass concentrations of the aerosol species between the satellite measurements and NICAM simulations. The annual averages of three compounds, i.e., sulfate, BC and POM, are compared over North America, Europe and Asia, whereas not only the annual averages but also the January and July averages dust and sea salt are compared at sites worldwide due to their large seasonal variabilities. The model results in both the HRM and the LRM exhibit a high correlation, low uncertainty and low bias, except for the relatively high negative bias for BC and POM with NMBs ranging from 46% to 56%. Although the differences in the statistical metrics between the HRM and LRM are very small, the metrics of the HRM are generally better than those of the LRM. The BC and most POM simulated in the NICAM are primary compounds that tend to be localized near the source region, so the simulated BC and POM distributions with the finer grid spacing are expected to be better. The differences in the simulated sulfate, which is a secondary component, between the HRM and LRM are caused both by differences in the transport of SO_2 and sulfate and by the cloud distributions related to sulfur chemistry (Goto et al., 2015b). The lower conversion ratio of the simulated precipitation to the simulated clouds (Figure 3(d)) in the HRM compared to that in the LRM result a longer lifetime for sulfate (Table 2) and provide larger values for the HRM-simulated sulfate. Even the HRM provides large underestimations of the simulated BC and POM, which is mainly because of their underestimation in China. The possible reasons for this phenomenon are probably the underestimation of BC and POM emissions and possibly the excessive localization of measured values. These findings are consistent with the results of the AOT underestimation in China (Figure 7).

The annual and January averages of both the HRM-simulated and the LRM-simulated dust mass concentrations at the available sites are comparable to the measurements. The correlations are high to moderate (the PCCs of the annual averages are approximately 0.9, and the PCCs of the January averages are approximately 0.65), the uncertainty is relatively small (the

https://doi.org/10.5194/gmd-2020-34
Preprint. Discussion started: 26 February 2020


Geoscientific Model Development Discussions

RMSEs of the annually averaged HRM- and LRM-simulated concentrations are less than 4 μg m^{-3}, while the January-averaged HRM-simulated concentration is 9 μg m^{-3}, and the January-averaged LRM-simulated concentration is 4 μg m^{-3}) and the bias is relatively low (the NMBs range from -22% to +37%). However, the uncertainty and bias in the July averages are higher than those in the annual and January averages, mainly because the emission fluxes from the Saharan and Arabian Deserts are larger in summer (July). The NMBs are calculated to be -64.8% (HRM) and -55.6% (LRM), the RMSEs are calculated to be 10.6 μg m^{-3} (HRM) and 10.2 μg m^{-3} (LRM), and the correlations are high (PCC=0.75 for the HRM and PCC=0.68 for the LRM).

For sea salt, the correlation is poor, except for the HRM in January, where the correlation is moderate with PCC=0.62. Since the emission fluxes of sea salt are strongly correlated with winds (the power of 3.41 mentioned in section 2.3), the differences in the simulated wind speeds shown in Figure 2 strongly affect the reproductivity of sea salt. The difference at the wind speed of 1.5 m s^{-1} provides the error in the sea salt emission flux of approximately 4. Therefore, a small error in the simulated wind speed can easily cause biases in the simulated sea salt emissions and its mass concentrations. Nevertheless, the bias and uncertainty of the NICAM-simulated sea salt are not large. The RMSE ranges from 7.7 to 8.2 μg m^{-3} for the HRM and from 7.9 to 10.6 μg m^{-3} for the LRM, while the NMB ranges from -29% to -18% for the HRM and from -41% to -31% for the LRM. Therefore, without nudging the meteorological fields, it is difficult to obtain results similar to the measurements in the sea salt simulation, even with the fine horizontal grid spacing of 14 km in this study.

In summary, both the HRM-simulated and the LRM-simulated aerosols are generally close to the MODIS-retrieved results and in-situ measurements, although the differences in the column burden between the HRM and LRM are found for sulfate (11.3%), WIBC (32.1%), POM (9.9%) and WSBC (10.4%). These are mainly caused by the modification of aerosol-cloud-precipitation interactions through wet deposition in the different horizontal grid spacings. The above verification of the relevant variables suggests that both the HRM and the LRM can be applied for a current global climate aerosol model. However, several important differences between the HRM and LRM have not been addressed in detail; therefore, section 4 discusses the remaining issues associated with using the HRM relative to the LRM.

https://doi.org/10.5194/gmd-2020-34
Preprint. Discussion started: 26 February 2020


Geoscientific Model Development Discussions

4 Discussion

In section 3, the modeled results using the HRM and LRM are shown as annual or monthly averages and/or global distributions of aerosol species using multiple measurements, i.e., MODIS, AERONET, IMPROVE, etc, against multiple variables, i.e., AOT and surface aerosol mass concentration for each aerosol component. This finding indicates that the results of both the HRM and the LRM are generally within the uncertainties of the measurements and other global models; furthermore, the differences in these variables between the HRM and LRM are not large in terms of the annual and global averages. However, some remarkable differences are found at the regional scale and in the results for sulfate and BC, but these differences and their mechanisms have not been thoroughly investigated. In section 4, more detailed comparisons are carried out to reveal both the differences in the simulated variables between the HRM and LRM and the advantages of using a HRM.

4.1 Effects of a fine grid spacing on aerosol fields

A high-resolution horizontal grid spacing has the potential to provide more realistic values of the model subgrid variability and possibly more realistic averages, for example, for aerosol concentrations in highly polluted areas, because most aerosols are emitted from heterogeneous hotspots on the surface. Figure 13 shows the mass concentrations of both BC and sulfate and the AOTs at the relevant sites, which are selected from the most polluted sites in the monthly averages within typical domains such as the United States, Europe and China. These results are derived from the results shown in Figures 7 and 11. In Figure 13, three sets of results are compared: the HRM with the original grid of 0.125°×0.125°, the HRM with the grid converted to 0.5°×0.5° and the LRM with the original grid of 0.5°×0.5°; hereafter, these models are referred to simply as HRM, HRM-0.5° and LRM, respectively. In section 3, comparisons of the aerosol mass concentrations and AOTs at the relevant sites are carried out using the model with the original grid size, but since an exact comparison using two models requires the same grid size, the HRM-0.5° is newly introduced in this section to clarify the differences caused only by the grid size. The results show that the HRM-simulated BC concentrations are the largest among the simulations since the BC is a primary aerosol and the relevant sites are located near BC emission sources. The HRM-0.5°-simulated BC concentrations

https://doi.org/10.5194/gmd-2020-34
Preprint. Discussion started: 26 February 2020

Geoscientific Model Development Discussions

are larger than the LRM-simulated BC concentrations. For example, during April in Chengdu, China, the simulated BC concentrations are 3.3 μgm^{-3} (HRM), 2.8 μgm^{-3} (HRM-0.5°) and 2.2 μgm^{-3} (LRM), which indicates that the difference among the simulated BC concentrations is approximately 35%. The differences, i.e., the relative ratios of the HRM-0.5° or LRM to the HRM, range from -63% (PHOE1, United States, December) to -2.5% (ATLA1, United States, September), with a median of -23%. Compared to the measurements, especially in China, even the HRM-simulated results tend to be underestimated. This is probably because the BC emission inventory in China is underestimated (e.g., Goto et al., 2015b), which may suggest the importance of using a much finer horizontal resolution in the simulation. For sulfate, which can serve as a representative secondary aerosol, and the AOT, which is highly influenced by RH, the HRM-simulated results are generally the best among the simulations, and the HRM-0.5°-simulated results are larger than the LRM-simulated results. For example, during August at BALT1 in the United States, the sulfate concentrations simulated by the HRM and HRM-0.5° range from 9.6 to 10.0 μgm^{-3}, whereas that simulated by the LRM is 0.9 μgm^{-3}, which is very different from the measurement (7.6 μgm^{-3}). The differences in the simulated sulfate concentrations among the simulations at all sites range from -91% (BALT1, United States, August) to +18% (ATLA1, United States, May), with a median of -4%. Underestimated simulated sulfate concentrations are also found in China and Vietnam, whereas such underestimations are not generally found in the United States or Europe. At some sites, the LRM-simulated AOTs are the largest among the simulations. These complex results imply complicated situations where the AOT depends on not only the aerosol burden but also the RH, whereas the BC mass concentration near the surface strongly depends on BC emissions. The differences in the simulated AOT concentrations among the simulations at all sites range from -49% (Nanging, China, August) to +223% (Nanging, China, August), with a median of -1%. The median values of the differences in the AOT among the simulations are smaller than those in sulfate by 3% and those in BC by 22%. Therefore, the differences in secondary and tertiary products among the different horizontal grid spacings cannot be explained simply by the grid size.

In addition to the impact of the model grid size on the monthly averages of the aerosol concentrations at the relevant sites, the temporal variations in the aerosol concentrations are also investigated. Such comparisons were carried out by Lin et al. (2017), who investigated the marine aerosol subgrid variability using a regional HRM over the southern Pacific Ocean. Lin et al. (2017) estimated variabilities in the aerosol mass concentrations of 15% near the surface and 50% in the free

https://doi.org/10.5194/gmd-2020-34
Preprint. Discussion started: 26 February 2020

troposphere in a 180-km×180-km domain using 3-hourly 3-km×3-km original grids for October 2008. In this study, these variabilities of the AOT, CCN at a height of 2 km, COT and precipitation are calculated in a 1°×1° domain using 6-hourly 14-km×14-km original grids for one year (Figure 14). The global and annual averages of the ratio for the AOT are calculated to be 28.5% (HRM) and 16.6% (LRM). The value obtained from only the HRM ranges between the two values obtained by Lin et al. (2017). For the CCN at a height of 2 km, the values are relatively small (7.6% for the HRM and 4.1% for the LRM), partly because the simulated CCN may be underestimated compared to the measurements, which show at least 100 cm^{-3} even over the oceans (e.g., Heintzenberg et al., 2000). Clouds and precipitation are also strongly influenced by subgrid variability (e.g., Pincus et al., 1999; Hakuba et al., 2013; Boutle et al., 2014). The global and annual averages of the ratio for the COT are calculated to be 80.0% (HRM) and 22.9% (LRM), whereas the global and annual averages of the ratio for precipitation are calculated to be 216.2% (HRM) and 77.9% (LRM). These values of clouds and precipitation are much larger than those obtained by aerosols. The relative differences in these parameters between the HRM and LRM are calculated to be 1.7 (AOT), 1.9 (CCN), 3.5 (COT) and 2.8 (precipitation). These results clearly indicate the importance of high-resolution simulations, especially for reproducing extreme phenomena related to aerosol, clouds and precipitation such as in the Amazon where the subgrid variabilities of both COT and precipitation in the HRM are high.

4.2 Arctic

Aerosols over the Arctic, especially BC, are incredibly important due to their impact on climate change (e.g., Willis et al., 2018). Unfortunately, it is generally difficult for global models to properly reproduce the aerosols over the Arctic (e.g., Shindell et al., 2008; Eckhardt et al., 2015; Sand et al., 2017). To solve this issue, many improvements to BC models have been applied by previous studies to microphysics processes, including aging and wet deposition processes (e.g., Liu et al., 2011; Lund and Berntsen, 2012; Marelle et al., 2017), and to the horizontal resolution to resolve the fine structures of clouds (e.g., Ma et al., 2014; Sato et al., 2016; Raut et al., 2017). Figure 16 illustrates the monthly variations in the BC and sulfate concentrations at three sites over the Arctic using four simulations: the HRM, LRM, LRM-macro (56-km grid spacing but using large-scale cloud condensation (Le Treut and Li, 1991) instead of the NSW6 cloud microphysics scheme and a

https://doi.org/10.5194/gmd-2020-34
Preprint. Discussion started: 26 February 2020


Geoscientific Model Development Discussions

cumulus parameterization (Chikira and Sugiyama, 2010) for the coarse grid spacing as a cloud macrophysics module) and very low-resolution NICAM model (220-km grid spacing used in Dai et al., 2014; Goto et al., 2015b; Dai et al., 2018; this simulation is called the VLRM-macro hereafter) with the cloud macrophysics module. Similar to previous studies (e.g., Shindell et al., 2008; Eckhardt et al., 2015; Sand et al., 2017), the LRM-macro- and VLRM-macro-simulated BC concentrations are also very different from the measurements. At Alert and Zeppelin, for example, the LRM-macro- and VLRM-macro simulated BC concentrations are highly underestimated, and the observed variation cannot be reproduced. However, both the HRM and the LRM with the cloud microphysics module succeed in simulating the observed seasonal variation (with the maximum in spring and the minimum in summer), but the HRM results are closer to the observations than the LRM results as a result of WIBC, as shown in Figure 9. At Barrow, the finer grid spacing of the LRM-macro-simulated BC provides better results than the VLRM-macro-simulated BC, but the former is still underestimated compared to the measurements, especially in spring. The good performance of the HRM and even the LRM can be found in the simulation of sulfate. Between the HRM and LRM, the largest difference in the surface BC mass concentrations between the HRM and LRM reaches 30% in spring. The differences in the simulated BC and sulfate concentrations between the HRM, LRM, LRM-macro and VLRM are mainly explained by differences in the cloud fraction and aerosol wet deposition, as shown in Sato et al. (2016). Near the aerosol source region, the simulated aerosol concentrations are strongly affected by their emission fluxes, but in remote areas such as the Arctic, aerosol wet deposition, which is directly related to cloud and precipitation processes, becomes important for their atmospheric lifetimes. In the LRM-macro and VLRM-macro simulations, the wet deposition process in winter results in unrealistic seasonal variations over the Arctic. The importance of wet deposition over the Arctic has also been noted by previous studies, such as Garrett et al. (2011), whose findings are consistent with our study. In addition, our results clearly show the importance of using numerical models with the cloud microphysics module, which introduces prognostic precipitation and does not diagnose the assumed cloud fraction used in the macrophysics cloud module. In summary, these processes related to hydrometeors and thus aerosol wet deposition strongly affect the aerosol simulations, especially over the Arctic.

https://doi.org/10.5194/gmd-2020-34
Preprint. Discussion started: 26 February 2020

Geoscientific Model Development Discussions

4.3 Vertical distributions of aerosols

Thus far, the horizontal distributions of the aerosols and their species are compared between the HRM and LRM and are validated using available measurements, but their vertical distributions are important for radiative forcings, especially BC (e.g., Haywood and Shine, 1997; Samset et al., 2013), although the model variability of BC is large (e.g., Textor et al., 2006; Kipling et al., 2016). Figure 16 shows the vertical profiles of the simulated and CALIPSO-retrieved aerosol extinction coefficients in 12 different regions, which are generally based on the definition in Koffi et al. (2016) by comparing Aerosol Comparisons between Observations and Models (AeroCom) models with CALIOP. The results of the HRM and LRM are generally comparable to those retrieved from CALIOP, but remarkable differences between the NICAM simulations and CALIOP retrievals are found in regions such as South America (panel k in Figure 16) and North Africa (panel h in Figure 16). In South America, the plume height is approximately 4 km in the NICAM simulations but approximately 2 km in the CALIOP measurements. As a result, both the HRM and the LRM are underestimated below a height of 3 km. This may be consistent with the AOT results shown in Figures 5 and 7, which show the underestimation of the AOT in the NICAM simulations compared to the MODIS and AERONET retrievals caused by the underestimation of biomass burning emissions or the overestimation of transport to upper-level areas. In northern Africa, where dust is a major component but the simulations exhibit large variabilities among the global models (e.g., Kim et al., 2014), both the HRM-simulated and the LRM-simulated extinction coefficients are overestimated compared to those retrieved from CALIOP, although the vertical profiles simulated by both the HRM and the LRM are comparable to those retrieved from CALIOP. This is also consistent with the overestimation of the AOT shown in Figures 5 and 7. The reason for this overestimation is probably attributed to the overestimation of dust emission fluxes in the NICAM simulations, which can be attributable to several sources: the overestimation of the wind speeds at a height of 10 m (Figure 2), the underestimation of soil moisture, and the failure to appropriately tune the models for dust emissions, although the global amount of emitted dust is within the variability estimated by other global models shown in Table 2. In addition, this finding suggests that the difference in the transport processes between different horizontal grid spacings is very small. Below a height of 5 km, the differences in the extinction coefficients between the HRM and LRM are small in all regions except for East China and the northwestern Pacific. It should be noted that the simulated extinction coefficient may not be overestimated above a height of 5 km, because optically

https://doi.org/10.5194/gmd-2020-34
Preprint. Discussion started: 26 February 2020


Geoscientific Model Development Discussions

thin aerosols are often undetected by CALIPO in the upper troposphere and the CALIOP regionally averaged extinction coefficient tends to be underestimated above 5 km (Watson-Parris et al., 2018).

Vertical observations of aerosol species are still limited, but recent measurements of vertical BC by flight campaigns such as HIPPO are available for a model evaluation (e.g., Schwarz et al., 2013; 2017; Samset et al., 2014; Lund et al., 2018). Figure 17 shows the NICAM-simulated vertical BC profiles and the measured vertical BC profiles from various missions in different regions: by flights in HIPPO for annual averages over the Pacific, by ARCTAS in spring and summer over the Arctic region where CALIOP does not generally detect aerosol signals, and by A-FORCE in spring over East Asia where anthropogenic BC is likely transported to the Arctic (and which can be an important source of BC over the Arctic) (e.g., Ikeda et al., 2017). The NICAM-simulated BC vertical profiles are generally comparable to those observed by flights and generally closer to the observations than other global models (Koch et al., 2009; Samset et al., 2014; Matsui and Mahowald, 2017; Kaiser et al., 2019; Tegan et al., 2019). Over the majority of the Pacific Ocean (60°S-60°N, 160°E-150°W), the NICAM-simulated BC concentrations shown as annual averages below a height of 3 km (approximately 700 hPa) in Figure 17 (a) to (c) are generally within the uncertainties obtained from the variability of the measurements, whereas the differences in the BC concentrations between the HRM and LRM are very small. Above approximately 700 hPa, however, the differences between the HRM and LRM become large, which is consistent with the results of the comparison with CALIOP in Figure 16. In addition, the HRM-simulated BC concentrations and even the LRM-simulated BC concentrations around the equator (20°S-20°N) are overestimated compared to the measurements, which has been noted by previous studies as one of the current problems among global aerosol models (e.g., Koch et al., 2009; Samset et al., 2014; Schwarz et al., 2017). The reason for this overestimation is possibly the overestimation of the BC atmospheric lifetime, which must be smaller than 5 days (Lund et al., 2018) but larger than 5 days in the HRM and other global models (Table 2). The overestimation of the BC lifetime may be attributed to the overestimation of the convective mass flux above 500 hPa, which may be improved by increasing the number of vertical layers in the model (Allen and Landuyt, 2014). Another possibility is a lack of secondary aerosol activation by convective clouds and associated removal by precipitation (Yu et al., 2019).

Over the Southern Ocean (60°S-80°S, 160°E-150°W), where the aerosols are transported from other areas, the observed BC concentrations are 10-50 ng kg^{-1} near the surface and more than 1 ng kg^{-1} at approximately 300 hPa. The surface BC

https://doi.org/10.5194/gmd-2020-34
Preprint. Discussion started: 26 February 2020


Geoscientific Model Development Discussions

concentrations are much lower than those in other areas, but those at 300 hPa are comparable to those in HIPPO-P2 (20°N-60°N) and HIPPO-P4 (60°S-20°S) and higher than those in HIPPO-P3 (20°S-20°N). These features of the observations are generally reproduced by the NICAM simulations, but the simulated BC concentrations tend to be overestimated compared to the measurements. Although previous studies offered only a limited discussion of BC transport to the Antarctic, this overestimation may be caused by the underestimation of BC wet deposition and possibly the overestimation of the horizontal transport of simulated BC to the Antarctic.

As discussed in section 4.2, both the HRM and the LRM successfully reproduce the aerosols over the Arctic. In Figure 17 (e), (g) and (h), where the vertical BC profiles over the Arctic region (>60°N) are shown, the NICAM-simulated BC concentrations near the surface are generally comparable to the measurements, except for the July-August average in panel (g). The observed BC concentrations in July-August seem to be inconsistent with the results in Figure 15, where the BC over the Arctic reaches a maximum concentration in spring (February-April) and a minimum in summer (June-October). This may be caused by specific smoke plumes during the observation period (Liu et al., 2011; Allen and Landuyt, 2014); however, these disturbances are not considered in our simulations since climatological emission fluxes are employed in this study. Actually, intensive biomass burning was observed in Russia and North America in the target year (2008) of the measurement period compared to the climatological years (Yasunari et al., 2018). In addition, the simulated BC concentrations in July-August are underestimated not only at the surface but also at all heights compared to the ARCTAS-B flight measurements. In the annual averages shown in panel (e), the simulated BC concentrations generally match the measurements, but above approximately 300 hPa, both the HRM and the LRM overestimate the BC concentrations, which is also the case in other regions (panels (a)-(d) in Figure 17). In spring (March-April) over the Arctic, both the HRM-simulated and the LRM-simulated BC concentrations are generally comparable to the measurements, even those obtained by flights (Figure 17(g)). In the main source regions of Arctic BC, i.e., East Asia, both the HRM-simulated and the LRM-simulated BC concentrations exhibit better agreement in the measurements (Figure 17(f)). In the middle troposphere (approximately 400-800 hPa) over the Arctic, however, both the HRM-simulated and the LRM-simulated BC concentrations are underestimated compared to the ARCTAS-A measurements. These findings may suggest that the HRM with O(10-km) grid spacing cannot resolve thee lifting process of aerosols at the Arctic front as pointed out by Quinn et al. (2011). Even when a source-receptor analysis of

https://doi.org/10.5194/gmd-2020-34
Preprint. Discussion started: 26 February 2020


Geoscientific Model Development Discussions

BC concentrations is used to identify the sources, the results remain highly uncertain, and no clear conclusions have been reached among previous studies. For example, Ikeda et al. (2017) employed the GEOS-Chem model and concluded that BC is mainly contributed by East Asian anthropogenic sources, whereas Matsui et al. (2011) used backward trajectories with both ARCTAS measurements and Weather Research and Forecasting (WRF) simulations and concluded that the BC over the Arctic is mainly contributed by biomass burning from Russia, North America and Europe. The differences between these models and measurements can be partly caused by a sampling problem without using exact grids and periods (Schutgens et al.,2016). In conclusion, a high-resolution grid system resolves one of the major issues regarding the distribution of BC, namely, the overestimation in the upper troposphere over the Pacific Ocean, but it does not solve the issue of its underestimation in the middle to upper troposphere over the Arctic.

4.4 Aerosol radiative forcing (ARF)

ARFs, which are complicated by various aerosol parameters, are the most important factors for estimating the impacts of aerosols on climate. Figure 18 shows the global and annual average ARFs due to the direct and indirect effects of anthropogenic and all aerosols under all-sky and clear-sky conditions. The direct ARFs due to anthropogenic aerosols under all-sky conditions are estimated to be -0.29 Wm^{-2} (HRM) and -0.24 Wm^{-2} (LRM), which are within the AeroCom estimates (from -0.58 Wm^{-2} to -0.02 Wm^{-2} with a mean of -0.20 Wm^{-2} and a standard deviation of 0.15 Wm^{-2} by Myhre et al., 2013) but slightly smaller than the estimation by the Max Planck Aerosol Climatology version 2 (MACv2) (-0.35 Wm^{-2}) by Kinne (2019). Under clear-sky conditions, the direct ARFs due to anthropogenic aerosols are estimated to be -0.57 Wm^{-2} (HRM) and -0.48 Wm^{-2} (LRM) , which are also within the AeroCom estimates (from -1.01 Wm^{-2} to -0.35 Wm^{-2} with a mean of -0.71 Wm^{-2} and a standard deviation of 0.18 Wm^{-2} by Myhre et al., 2013) but smaller than the MACv2 estimate (-0.69 Wm^{-2}) by Kinne (2019). The differences in the ARFs between the HRM and LRM under both all- and clear-sky conditions are within 0.1 Wm^{-2}, which is smaller than the standard deviation among the AeroCom models. The direct ARFs due to all aerosols, i.e., anthropogenic and natural aerosols, under all-sky conditions are estimated to be -1.80 Wm^{-2} (HRM) and -1.70 Wm^{-2} (LRM). For only shortwave fluxes, the ARFs are estimated to be -2.03 Wm^{-2} (HRM) and -1.93 Wm^{-2} (LRM), which are comparable to the measurement-based estimates using CALIOP (Oikawa et al., 2018) and MACv2 (Kinne, 2019) within approximately

https://doi.org/10.5194/gmd-2020-34
Preprint. Discussion started: 26 February 2020


Geoscientific Model Development Discussions

0.2 Wm^{-2} but smaller than the assimilated estimate of -3.1 Wm^{-2} (Su et al., 2013). Table 3 shows the TOA and surface components of the ARFs under all-sky and clear-sky conditions. First, the largest difference in the TOA ARF between the HRM and LRM under all-sky conditions is found for sulfate (-0.06 Wm^{-2}), whereas the differences in the other components between the HRM and LRM are within 0.02 Wm^{-2}. This is also consistent with the differences in the AOT and column burden shown in Figures 8 and 9. Second, the largest difference in the surface ARF between the HRM and LRM under all-sky conditions is found for WIBC (-0.07 Wm^{-2}), whereas that in the TOA ARF is only 0.02 Wm^{-2}. Under clear-sky condition, the largest difference in the ARF for WIBC is approximately 0 Wm^{-2} at the TOA and -0.08 Wm^{-2} at the surface. The differences in the ARF at the surface are consistent with those in the column burden of WIBC; thus, these differences between the TOA and surface can be explained by the stratification of WIBC and clouds (e.g., Haywood and Shine, 1997). Although the differences in the ARF due to BC between the HRM and LRM are found, both the HRM and LRM estimated a positive ARF due to the WIBC and even the WSBC seems to be underestimated compared to the observation-based studies by Oikawa et al. (2018) and Kinne (2019). This is supported by the fact that the differences in the ARF between all-sky and clear-sky conditions are lower than those by Oikawa et al. (2018) and Kinne (2019), probably because the light-absorption amount of carbonaceous aerosols under the cloudy condition is underestimated due to the underestimation of clouds. Third, the shortwave ARFs due to all aerosols at the surface under all-sky conditions are estimated to be -3.37 Wm^{-2} (HRM) and -3.27 Wm^{-2} (LRM), the absolute values of which are smaller than those in previous studies based on satellites (-4.23 Wm^{-2} to -7.79 Wm^{-2}, summarized by Korras-Carraca et al., 2019) and the MACv2 estimate (-4.0 Wm^{-2}) by Kinne (2019). This is probably because the dust shortwave ARFs in both the HRM and the LRM have the largest negative values among the aerosol species due to the overestimation of the single scattering albedo (SSA) over desert areas (0.96-0.97 in this study) compared to other studies based on AERONET retrievals (0.92 in Giles et al., 2012). Another reason is the underestimation of ground surface albedo, which is a tendency of the NICAM, and our previous study (Dai et al., 2018) also showed negative ARF values even over the desert area. Fourth, the ARF due to sea salt under all-sky conditions is estimated to be approximately -0.48 Wm^{-2} (in both the HRM and the LRM), which is comparable to the values reported in previous studies (-0.21 Wm^{-2} to -2.21 Wm^{-2} in Partanen et al., 2014; -0.31 Wm^{-2} in Takemura et al., 2002; -0.55 Wm^{-2} in Jacobson, 2001),

https://doi.org/10.5194/gmd-2020-34
Preprint. Discussion started: 26 February 2020


Geoscientific Model Development Discussions

even though the simulated AOTs over the oceans tend to be larger than the satellite results. Again, this gap in the ARFs between the model-based and observation-based estimates cannot be solved by using a finer grid resolution in global models. By using a method proposed by Ghan (2013), the ARFs due to the anthropogenic IARF are estimated to be -0.93 Wm^{-2} (HRM) and -1.10 Wm^{-2} (LRM). These values are comparable to those in another study (-1.06 Wm^{-2}) by Jing and Suzuki (2018) and slightly larger than the values published in the Fifth Assessment Report by the Intergovernmental Panel on Climate Change (IPCC-AR5) (-0.45 Wm^{-2} with a 90% uncertainty range from 0 Wm^{-2} to -1.2 Wm^{-2}), albeit within uncertainty. However, it should be noted that our estimates are still uncertain. First, this is because the biomass burning emissions in this study are assumed to be zero during the preindustrial era. Second, the minimum CCN value in this study is set at 25 cm^{-1}, which strongly affects the ARF due to the IARF (Hoose et al., 2009). Third, the meteorological variability among different years can influence the results, as discussed in section 4.5. Furthermore, the magnitude of the difference between the HRM and LRM is estimated to be 0.17 Wm^{-2}, which is larger than that of the ARF due to the aerosol direct effect. The HRM-simulated IARF is generally lower than the LRM-simulated IARF, which is partly explained by the following: the HRM-simulated CCN concentrations are larger than the LRM-simulated CCN concentrations (Figure 14), and the IARF generally becomes smaller as the aerosol concentrations become larger (e.g., Carslaw et al., 2013). In the total effect, because some of the ARFs are canceled out, the difference due to both direct and indirect effects attributable to direct forcing in the HRM is calculated to be -0.11 Wm^{-2}.

4.5 Uncertainties caused by meteorological fields

The variabilities of aerosols caused by the meteorological fields are discussed and quantified by comparing the differences between the HRM and LRM. Figure 19 shows the magnitudes of the differences in the emission fluxes for dust and sea salt, column aerosol burdens, the AOT, and the direct ARF at the TOA between the HRM and LRM or between the 3-year integrations in the HRM and LRM. For the emitted sea salt, for example, the difference between the HRM and LRM is estimated to be 911 Tg yr^{-1}, which is much larger than the difference in the variability of the 3-year meteorological fields (155 Tg yr^{-1} for the HRM and 241 Tg yr^{-1} for the LRM). Therefore, the impact of the horizontal grid size on sea salt emissions is larger than that caused by meteorological variability over 3 years. In contrast, the difference in emitted dust

https://doi.org/10.5194/gmd-2020-34
Preprint. Discussion started: 26 February 2020


Geoscientific Model Development Discussions

between the different horizontal resolutions is within the range of the difference caused by meteorological variabilities over 3 years in the HRM and LRM. These may be explained by differences in the simulated winds, which are strongly affected by the simulated surface temperature; the SST is fixed, but the temperature over land is a diagnostic variable. Therefore, the differences in the column burden and AOT for dust are within the range of the differences caused by meteorological variabilities. The difference in the column burden for sea salt is slightly larger than that for dust, but the difference in the AOT for sea salt is within the range of the difference caused by meteorological variabilities. The differences in the column burden and AOT for sulfate between the HRM and LRM are larger than those caused by meteorological variabilities, indicating that the difference in the clouds between the different horizontal grid spacings (14 km versus 56 km) is larger than that among the meteorological variabilities with the same horizontal grid spacings. This conclusion is also applicable to the carbonaceous parameters, but the difference in the AOT for carbon between the HRM and LRM is comparable to that among the meteorological variabilities in the HRM. As a result, the difference in the AOT between the HRM and LRM is smaller than that among the meteorological variabilities. For the DARF, the differences in the total ARFs under both conditions between the HRM and LRM are larger than those among the meteorological variabilities, whereas the differences in the longwave or shortwave DARFs under cloudy conditions, which are strongly related to clouds, are generally smaller than those among the meteorological variabilities. Therefore, discussions of the impacts of different horizontal grid spacings on the total AOT and DARF under cloudy conditions or for longwave ARFs are difficult to facilitate using only a 1-year integration.

5 Summary

What is the advantage of an *actual* HRM with aerosols? To address this question, we developed a global aerosol transport model on NICAM.16 with a 14-km horizontal grid spacing. Previous studies have spent considerable amounts of resources to find the answer, but all of these studies were limited in terms of the domain (regional or urban scale) and period (several days to 1 month). Although previous studies focused on the global scale, the horizontal grid spacing was still coarse, i.e., more than 50 km. In this study, we execute a global cloud-system resolving model, NICAM, coupled to aerosol components with a 14-km grid spacing and evaluate the simulated aerosol distributions, their budgets and their interactions with clouds

https://doi.org/10.5194/gmd-2020-34
Preprint. Discussion started: 26 February 2020


Geoscientific Model Development Discussions

against multiple measurements and other models. For comparison, we also execute the NICAM simulations with a 56-km grid spacing as an LRM, which still boasts a high resolution among the current global aerosol models. The integration time is 3 years, which is very long with such a HRM. Therefore, this work represents a very pioneering study.

The relevant variables, i.e., wind, clouds and precipitation, that strongly determine the aerosol distributions are evaluated using reanalysis data, satellite and in situ measurements. The differences in the global and annual averages between the HRM and LRM are within 10%, and both differences generally range within the uncertainties of the measurements and other global models. Our specific conclusions are described below.

- We expected the HRM-simulated wind speeds to be higher than the LRM-simulated wind speeds, but this is not always the case.
- The HRM-simulated clouds (cloud fraction and cloud optical thickness) are smaller than the LRM-simulated clouds because the LRM tends to reproduce unrealistically strong convective clouds compared to the HRM. Such convective clouds can provide strong precipitation due to the coarseness of the horizontal grid spacing. However, the clouds simulated by the HRM and LRM are not underestimated compared to the MODIS retrievals.
- The HRM-simulated RPCW, which is very important for determining the aerosol wet removal rate, is smaller than that simulated by the LRM by approximately 20%, which means the LRM-simulated aerosols are more quickly scavenged by precipitation than the HRM-simulated aerosols.
- Both the HRM-simulated and the LRM-simulated TOA shortwave radiative fluxes are closer to the satellite measurements by CERES than are the results of a previous study using NICAM simulations with a 14-km grid spacing but without aerosol components (Kodama et al., 2015). The bias is less than 8 Wm^{-2}, which is within the uncertainty among global models. However, the LRM reproduces the CERES-estimated radiative fluxes better than the HRM due to the larger clouds in the LRM.
- At the surface, the BSRN-observed global radiation fluxes are sufficiently reproduced by both the HRM and the LRM (PCC=0.9, NMB<1%, RMSE=-32 Wm^{-2}), although diffuse and direct radiations have higher biases and uncertainties reaching up to 30% of the NMB.

The conclusions for the simulated aerosol evaluations are described below.

https://doi.org/10.5194/gmd-2020-34
Preprint. Discussion started: 26 February 2020

- Both the HRM-simulated and the LRM-simulated AOTs are generally close to the MODIS-retrieved AOTs with PCC>0.4, RMSE=0.15 and NMB<10%. A comparison using in situ measurements shows that the HRM-simulated AOTs are slightly closer to the measurements than are the LRM-simulated AOTs, as the former have a higher correlation (PCC=0.47), lower uncertainty (RMSE=0.21) and lower bias (-20%).
- The analysis of the chemical components for the AOTs and column burdens shows that the largest difference in AOTs between the HRM and LRM is found for sulfate (15.7%), followed by carbon (5.2%). Large differences in the column burden are found for sulfate (11.3%), WIBC (32.1%), POM (9.9%) and WSBC (10.4%). Differences in sulfate and WIBC occur over a large area.
- The global budgets of aerosol species in both the HRM and the LRM generally range within those obtained from other global models, except for the atmospheric lifetime of sulfate, whose lifetime is estimated to be 2.4 days (HRM) and 2.1 days (LRM), respectively, whereas it ranges from 3.3 days to 4.9 days in other global models. This tendency is also found for sea salt, whose lifetime is 0.23 days (HRM) and 0.21 days (LRM), whereas it ranges from 0.2 days to 1.0 day in other global models. Between the HRM and LRM, some remarkable differences in the wet deposition flux of sea salt and the lifetime of BC of more than 20% are observed. These results suggest that aerosol-cloud-precipitation interactions through wet deposition are modified in the models with different horizontal resolutions and the HRM will provide better results.
- The simulated surface aerosols for fine-mode particles such as sulfate, POM and BC are generally in agreement with the measurements, except in China, where the simulated results are underestimated. This suggests that the 14-km grid spacing is not sufficient to resolve such high concentrations in highly dense urban areas.
- The simulated surface aerosols for dust are generally in agreement in the measurements but not for sea salt. This is probably because the slight bias in the wind causes considerable bias in the sea salt emission flux; i.e., the 1.5 m s^{-1} difference in the wind speed at a height of 10 m provides a 4-fold difference in the sea salt emission flux.

The verification of the relevant variables suggests that both the HRM and the LRM can be applicable for a current global climate aerosol model. However, several important differences between the HRM and LRM have not been addressed in detail; therefore, section 4 discusses the following six issues to clarify the remaining issues relative to the LRM.

https://doi.org/10.5194/gmd-2020-34
Preprint. Discussion started: 26 February 2020


Geoscientific Model Development Discussions

What is the impact of the high-resolution grid on the coarse-grid average used in global aerosol models (section 4.1)?

At the relevant sites, the variabilities are -23% (-63% to -2.5%) for surface BC, -4% (-91% to +18%) for surface sulfate and -1% (-49% to +223%) for AOT. On a global scale, the variabilities in the AOT are calculated to be 28.5% (HRM) and 16.6% (LRM); i.e., the ratio between the HRM and LRM is 1.7. For CCN, COT and precipitation, the ratios are calculated to be 1.9, 3.5 and 2.8, respectively. This clearly shows how the HRM reproduces such variability in relation to extreme weather phenomena.

What is the impact of the high-resolution grid on the reproductivity of BC and sulfate over the Arctic (section 4.2)?

Unlike previous global models and our model with a lower grid spacing and a cloud macrophysics module, both the HRM and the LRM succeed in reproducing the observed BC and sulfate over the Arctic. Between the HRM and LRM, the difference in the BC concentration reaches 30% in spring, and the HRM results are better than the LRM results. Our sensitivity experiments show the importance of considering cloud microphysics processes, including prognostic precipitation, which is one of the processes related to the wet deposition of aerosols, as suggested by previous studies.

What is the impact of the high-resolution grid on the vertical distribution of aerosols (section 4.3)?

The differences in the column burdens influence sulfate and carbonaceous aerosols, but the corresponding changes in the vertical distribution are not discussed in section 3. Using CALIOP/CALIPSO satellite observations, both the HRM and the LRM generally reproduce the vertical profiles of the CALIOP-retrieved aerosol extinction coefficients worldwide. The issue regarding the overestimation of aerosols in the middle troposphere among the current global aerosol models is not found extensively in this study. However, the use of a high-resolution grid does not resolve one of the major issues pertaining to the BC distribution: the underestimation in the middle to upper troposphere over the Arctic. In the middle and upper troposphere, especially above 3 km, the HRM-simulated aerosol concentrations tend to be higher than the LRM-simulated concentrations, and the HRM results are overestimated compared to the CALIOP measurements. The analysis of the column burden indicates that this difference is caused by WIBC and sulfate. This and the finding that the differences in the vertical profiles over dusty regions are very small suggest that wet deposition processes rather than the transport characteristics cause the differences in the vertical profiles between the HRM and LRM.

How are the ARFs modified by using the HRM (section 4.4)?

https://doi.org/10.5194/gmd-2020-34
Preprint. Discussion started: 26 February 2020


Geoscientific Model Development Discussions

The ARFs estimated from both the HRM and the LRM are within the uncertainties obtained from the observations and other global models. The largest difference in the ARFs between the HRM and LRM is 0.05 Wm^{-2} at TOA for sulfate and 0.07 Wm^{-2} at the surface for WIBC. Even though the differences in the ARF due to BC between HRM and LRM are found, both HRM and LRM estimated positive ARF due to WIBC and even WSBC seems to be underestimated, compared to the observation-based studies by Oikawa et al. (2018) and Kinne (2019). Both the HRM-estimated and the LRM-estimated ARFs due to dust are negatively larger than those in other models because of the overestimation of the SSA and the underestimation of the surface albedo over desert areas. The negatively large dust-related ARF is responsible for the underestimation of the surface ARF compared to the satellite results. For the ARF due to anthropogenic aerosol indirect forcing (i.e., the IARF), the difference between the HRM and LRM is 0.17 Wm^{-2}, which is larger than that obtained for the direct aerosol forcing. This study indicates that a higher-resolution model provides a lower IARF that is closer to the reference value shown in the IPCC-AR5. However, it should be noted that several important assumptions used in this study can affect the IARF values, so this process must be further developed and refined to properly estimate the IARF.

Is the difference between the HRM and LRM larger than the variability among the different meteorological fields obtained by the 3-year integration (section 4.5)?

The relevant variables, i.e., the sea salt emission flux, column burdens for sulfate and carbon, including POM and BC, and total DARF, are influenced by the horizontal resolution, but the others, i.e., the dust emission fluxes, AOT, and longwave and shortwave DARFs under cloudy conditions, are strongly influenced by the variabilities caused by the meteorological fields.

Finally, the following question “How high is the calculation cost when using the HRM?” is considered. This answer is balanced by the precision of the aerosol simulation. Actually, the computer resources required by the HRM are more than ten times higher than that required by the LRM when using the same supercomputer with the same number of processers. When focusing on extreme phenomena related to clouds and precipitation and ACIs, a 14-km grid spacing (or finer) is needed to clearly resolve the scientific questions addressed in this study. In this case, various parameters associated with the aerosol distributions are well tuned using the LRM (56-km grid) for the HRM (14-km grid) simulations under the limitation of the available computational resources. In contrast, when focusing on the general circulations of aerosols and related gases, a 56-

https://doi.org/10.5194/gmd-2020-34
Preprint. Discussion started: 26 February 2020


Geoscientific Model Development Discussions

km grid spacing with a cloud microphysics module is sufficient, and the results are similar to those with a 14-km grid spacing (with a difference of 10% on a global average). If the available computational resources greatly increase in the near future, we hope these suggestions will become helpful for all modelers.

Code and data availability

The source codes of NICAM.16 can be obtained upon request under the general terms and conditions (http://nicam.jp/hiki/?Research+Collaborations). The data that support the findings of this study can be archived with DOI:10.5281/zenodo.3687323.

Author contribution

DG designed and operated the numerical experiments and analyses. YS, HY and KS coordinated the model configuration and prepared the external conditions of the experiments. RK, EO, and TMN prepared the observational datasets for the model evaluation. TN submitted the proposal for the computational resources. DG wrote the initial draft of the paper, and all coauthors participated in discussions over the results and commented on the original manuscript.

Competing interests

The authors declare that they have no conflicts of interest.

https://doi.org/10.5194/gmd-2020-34
Preprint. Discussion started: 26 February 2020

Geoscientific Model Development Discussions

Acknowledgements

We acknowledge the developers and administrators of NICAM (http://nicam.jp/), SPRINTARS (https://sprintars.riam.kyushu-u.ac.jp/indexe.html), and MODIS (https://modis.gsfc.nasa.gov/) and the relevant PIs of the AERONET (https://aeronet.gsfc.nasa.gov/), SKYNET (https://www.skynet-isdc.org/) and CARSNET sites. We are grateful to the NCEP-FNL group, the NCEP/National Weather Service/National Oceanic Atmospheric Administration (NOAA)/U.S. Department of Commerce (2000), the NCEP FNL Operational Model Global Tropospheric Analyses (continuing from July 1999), https://doi.org/10.5065/D6M043C6, and the NCAR Research Data Archive, Computational and Information Systems Laboratory, Boucher, Colo. (updated daily), last accessed 4 January 2020. The CERES datasets were obtained from the NASA LaRC Atmospheric Science Data Center. Some of the authors were supported by the Environment Research and Technology Development Fund (S-12) of the Environmental Restoration and Conservation Agency, Japan, and by JSPS KAKENHI grants (26740010, 15K17766, 17H04711, 19H05669). Additionally, we were supported by the following projects: the Ministry of Environment (MOE)/GOSAT, the Japan Science and Technology (JST), CREST/EMS/TEEDDA, JAXA/EarthCARE, JAXA/GCOM-C, and NIES. The model simulations were performed using supercomputers: the K computer (hp160004, hp160231, hp170017, hp170232, hp180012, and hp180181), NIES/NEC SX-ACE and JAXA/JSS2. We also acknowledge Drs. H. Matsui (Nagoya University), T. Seiki (JAMSTEC) and K. Ikeda (NIES) for their discussions and Profs. Y. Kondo (National Institute of Polar Research in Japan), M. Koike (University of Tokyo), and N. Moteki (University of Tokyo) and the NOAA Black Carbon Group for providing us with their aircraft BC measurements. Global maps in the figures are drawn using Grid Analysis and Display System (GrADS) (http://cola.gmu.edu./grads/).

References

Abdul-Razzak, H., and Ghan, S. J.: A parameterization of aerosol activation: 2 Multiple aerosol types, J. Geophys. Res., 105, D5, 6837-6844, doi:10.1029/1999JD901161, 2000.

https://doi.org/10.5194/gmd-2020-34
Preprint. Discussion started: 26 February 2020

Adler, R. F., Huffman, G. J., Chang, A., Ferraro, R., Xie, P., Janowiak, J., Rudolf, B., Schneider, U., Curtis, S., Bolvin, D., Gruber, A., Susskind, J., and Arkin, P.: The version 2 Global Precipitation Climatology Project (GPCP) monthly precipitation analysis 1979-present, J. Hydrometeorol., 4, 1147-1167, doi:10.1175/1525-7541(2003)004<1147:TVGPCP>2.0.CO;2, 2003.

Bates, T. S., Charlson, R. J., and Gammon, R. H.: Evidence for the climate role of marine biogenic sulphur, Nature, 329, 319–321, 1987.

Berry, E. X.: Cloud droplet growth by collection, J. Atmos. Sci., 24, 688-701, 1967.

Bond, T. C., Doherty, S. J., Fahey, D. W., Forster, P. M., Berntsen, T., DeAngelo, B. J., Flanner, M. G., Ghan, S., Kärcher, B., Koch, D., Kinne, S., Kondo, Y., Quinn, P. K., Sarofim, M. C., Schultz, M. G., Schulz, M., Venkataraman, C., Zhang, H., Zhang, S., Bellouin, N., Guttikunda, S. K., Hopke, P. K., Jacobson, M. Z., Kaiser, J. W., Klimont, Z., Lohmann, U., Schwarz, J. P., Shindell, D., Storelvmo, T., Warren, S. G., and Zender, C. S.: Bounding the role of black carbon in the climate system: A scientific assessment, J. Geophys. Res.: Atmos., 118, 1-173, doi:10.1002/jgrd.50711, 2013.

Boutle, I. A., Abel, S. J., Hill, P. G., and Morcrette, C. J.: Spatial variability of liquid cloud and rain: observations and microphysical effects, Q. J. R. Meteorol. Soc., 140, 583-594, doi:10.1002/qj.2140, 2014.

Carslaw, K. S., Lee, L. A., Reddington, C. L., Pringle, K. J., Rap, A., Forster, P. M., Mann, G. W., Spracklen, D. V., Woodhouse, M. T., Regayre, L. A., and Pierce, J. R.: Large contribution of natural aerosols to uncertainty in direct forcing, Nature, 503, 67-71, doi:10.1038/nature12674, 2013.

Che, H., Zhang, X.-Y., Xia, X., Goloub, P., Holben, B., Zhao, H., Wang, Y., Zhang, X.-C., Wang, H., Blarel, L., Damiri, B., Zhang, R., Deng, X., Ma, Y., Wang, T., Geng, F., Qi, B., Zhu, J., Yu, J., Chen, Q., and Shi, G.: Ground-based aerosol climatology of China: aerosol optical depths from the China Aerosol Remote Sensing Network (CARSNET) 2002–2013, Atmos. Chem. Phys., 15, 7619–7652, doi:10.5194/acp-15-7619-2015, 2015.

Chung, S. H., and Seinfeld, J. H.: Global distribution and climate forcing of carbonaceous aerosols, J. Geophys. Res., 107(D19), 4407, doi:10.1029/2001JD001397, 2002.

https://doi.org/10.5194/gmd-2020-34
Preprint. Discussion started: 26 February 2020

Chikira, M., and Sugiyama, M.: A Cumulus Parameterization with State-Dependent Entrainment Rate. Part I: Description and Sensitivity to Temperature and Humidity Profiles, J. Atmos. Sci., 67, 2171–2193, doi:10.1175/2010JAS3316.1, 2010.

Dai, T., Goto, D., Schutgens, N. A. J., Dong, X., Shi, G., and Nakajima, T.: Simulated aerosol key optical properties over global scale using an aerosol transport model coupled with a new type of dynamic core, Atmos. Environ., 82, 71-82, doi: 10.1016/j.atmosenv.2013.10.018, 2014.

Dai, T., Cheng, Y., Zhang, P., Shi, G., Sekiguchi, M., Suzuki, K., Goto, D., and Nakajima, T.: Impacts of meteorological nudging on the global dust cycle simulated by NICAM coupled with an aerosol model, Atmos. Environ., 190, 99-115, doi:10.1016/j.atmosenv.2018.07.016, 2018.

Diehl, T., Heil, A., Chin, M., Pan, X., Streets, D., Schulz, M., and Kinne, S.: Anthropogenic, biomass burning, and volcano emissions of black carbon, organic carbon, and SO_2 from 1980 to 2010 for hindcast model experiments, Atmos. Chem. Phys. Discuss., 12, 24895-24954, doi:10.5194/acpd-12-24895-2012, 2012.

Eckhardt, S., Quennehen, B., Olivié, D. J. L., Berntsen, T. K., Cherian, R., Christensen, J. H., Collins, W., Crepinsek, S., Daskalakis, N., Flanner, M., Herber, A., Heyes, C., Hodnebrog, Ø., Huang, L., Kanakidou, M., Klimont, Z., Langner, J., Law, K. S., Lund, M. T., Mahmood, R., Massling, A., Myriokefalitakis, S., Nielsen, I. E., Nøjgaard, J. K., Quaas, J., Quinn, P. K., Raut, J.-C., Rumbold, S. T., Schulz, M., Sharma, S., Skeie, R. B., Skov, H., Uttal, T., von Salzen, K., and Stohl, A.: Current model capabilities for simulating black carbon and sufate concentrations in the Arctic atmosphere: a mulit-model evaluation using a comprehensive measurement data set, Atmos. Chem. Phys., 15, 9413-9433, doi:10.5194/acp-15-9413-2015, 2015.

Ezzati, M., Lopez, A.D., Rodgers, A., Vander Hoorn, S., Murray, C.J., and Comparative Risk Assessment Collaborating Group: Selected major risk factors and global and regional burden of disease, Lancet, 360, 1347–1360. doi:10.1016/S0140-6736(02)11403-6, 2002.

Galmarini, S., Kioutsioukis, I., Solazzo, E., Alyuz, U., Balzarini, A., Bellasio, R., Benedictow, A. M. K., Bianconi, R., Bieser, J., Brandt, J., Christensen, J. H., Colette, A., Curci, G., Davila, Y., Dong, X., Flemming, J., Francis, X., Fraser, A., Fu, J., Henze, D., Hogrefe, C., Im, U., Vivanco, M. G., Jimenez-Guerrero, P., Jonson, J. E., Kitwiroon, N., Manders,

https://doi.org/10.5194/gmd-2020-34
Preprint. Discussion started: 26 February 2020

A., Mathur, R., Palacios-Pena, L., Pirovano, G., Pozzoli, L. , Prank, M., Schultz, M., Sokhi, R. S., Sudo, K., Tuccella, P., Takemura, T., Sekiya, T., and Unal, A.: Two-scale multi-model ensemble: Is a hybrid ensemble of opportunity telling us more?, Atmos. Chem. Phys., 18, 8727–8744, doi:10.5194/acp-18-8727-2018, 2018.

Garrett, T. J., Brattström, S., Sharma, S., Worthy, D. E. J., Novelli, P.: The role of scavenging in the seasonal transport of black carbon and sulfate to the Arctic. Geophys. Res. Lett. 38, L16805, doi: 10.1029/2011GL048221, 2011.

Ghan, S.J.: Technical Note: Estimating aerosol effects on cloud radiative forcing, Atmos. Chem. Phys., 13, 9971-9974, doi:10.5194/acp-13-9971-2013, 2013.

Ghan, S. J., Leung, L. R., Easter, R. C., and Abdul-Razzak, A.: Prediction of cloud droplet number in a general circulation model, J. Geophys. Res., 102, 21,777–21,794, 1997.

Giles, D. M., Holben B. N., Eck, T. F., Sinyuk, A., Smirnov, A., Slutsker, I., Dickerson, R. R., Thimpson, A. M., and Schafer, J. S.: An analysis of AERONET aerosol absorption properties and classifications representative of aerosol source regions, J. Geophys. Res., 117, D17203, doi:10.1029/2012JD018127, 2012.

Goto, D., Nakajima, T., Takemura, T., and Sudo, K.: A study of uncertainties in the sulfate distribution and its radiative forcing associated with sulfur chemistry in a global aerosol model, Atmos. Chem. Phys., 11, 10889-10910, doi:10.5194/acp-11-10889-2011, 2011.

Goto, D., Oshima, N., Nakajima, T., Takemura, T., and Ohara, T.: Impact of the aging process of black carbon aerosols on their spatial distribution, hygroscopicity, and radiative forcing in a global climate model, Atmos. Chem. Phys. Discuss., 12, 29801-29849, doi:10.5194/acpd-12-29801-2012, 2012.

Goto, D., Dai, T., Satoh, M., Tomita, H., Uchida, J., Misawa, S., Inoue, T., Tsuruta, H., Ueda, K., Ng, C.F.S., Takami, A., Sugimoto, N., Shimizu, A., Ohara, T., and Nakajima ,T.: Application of a global nonhydrostatic model with a stretched-grid system to regional aerosol simulations around Japan, Geosci. Model Dev., 8, 235-259. doi:10.5194/gmd-8-235-2015, 2015a.

Goto D., Nakajima, T., Dai, T., Takemura, T., Kajino, M., Matsui, H., Takami, A., Hatakeyama, S., Sugimoto, N., Shimizu, A., and Ohara, T.: An evaluation of simulated particulate sulfate over East Asia through global model intercomparison, J. Geophy. Res. Atmos., 120, 6247-6270, doi:10.1002/2014JD021693, 2015b.

https://doi.org/10.5194/gmd-2020-34
Preprint. Discussion started: 26 February 2020

Goto, D., Ueda, K., Ng, C.F.S., Takami, A., Ariga, T., Matsuhashi, K., and Nakajima, T.: Estimation of excess mortality due to long-term exposure to PM2.5 in Japan using a high-resolution model for present and future scenarios. Atmos. Environ. 140, 320-332. doi:10.1016/j.atmosenv.2016.06.015, 2016.

Goto, D., Sato, Y., Yashiro, H. & Suzuki, K. Validation of high-resolution aerosol optical thickness simulated by a global non-hydrostatic model against remote sensing measurements. AIP Conference Proceedings 1810, 100002, 2017.

Goto D., Nakajima, T., Dai, T., Yashiro, H., Sato, Y., Suzuki, K., Uchida, J., Misawa, S., Yonemoto, R., Trieu, T.T.N., Tomita, H., and Satoh, M.: Multi-scale Simulations of Atmospheric Pollutants Using a Non-hydrostatic Icosahedral Atmospheric Model. In: Vadrevu K., Ohara T., Justice C. (eds) Land-Atmospheric Research Applications in South and Southeast Asia. Springer Remote Sensing/Photogrammetry. Springer, Cham, 2018

Goto, D., Kikuchi, M., Suzuki, K., Hayasaki, M., Yoshida, M., Nagao, T. M., Choi, M., Kim, J., Sugimoto, N., Shimizu, A., Oikawa, E., and Nakajima, T.: Aerosol model evaluation using two geostationary satellites over East Asia in May 2016, Atmos. Res., 217, 93-113, doi:10.1016/j.atmosres.2018.10.016, 2019.

Grythe, H., Ström, Krejci, R., Quinn, P., and Stohl, A.: A review of sea-spray aerosol source functions using a large global set of sea salt aerosol concentration measurements, Atmos. Chem. Phys., 1277-1297, doi:10.5194/acp-14-1277-2014, 2014.

Guenther, A., Hewitt, C. N., Erickson, D., Fall, R., Geron, C., Graedel, T., Harley, P., Klinger, L., Lerdau, M., McKay, W. A., Pierce, T., Scholes, B., Steincrecher, R., Tallamraju, R., Taylor, J., and Zimmerman, P. A.: Global-Model of Natural Volatile Organic-Compound Emissions, J. Geophys. Res., 100, 8873–8892, 1995.

Hakuba, M. Z., Folini, D., Sanchez-Lorenzo, A., and Wild, M.: Spatial representativeness of ground-based solar radiation measurements, J. Geophys. Res., 118, 8585-8597, doi:10.1002/jgrd.50673, 2013.

Haywood, J. M., and Shine, K. P.: Multi-spectral calculations of the radiative forcing of tropospheric sulphate and soot aerosols using a column model, Quart. J. R. Meteor. Soc., 123, 1907-1930, 1997.

Heintzenberg, J., Covert, D. C., van Dingenen, R.: Size distribution and chemical composition of marine aerosols: a compilation and review, Tellus, 52B, 4, 1104-1122, 2000.

https://doi.org/10.5194/gmd-2020-34
Preprint. Discussion started: 26 February 2020

Holben, B. N., Eck, T. F., Slutsker, I., Tanré, D., Buis, J. P., Setzer, A., Vermote, E., Reagan, J. A., Kaufman, Y., Nakajima, T., Lavenu, F., Jankowiak, I., and Smirnov, A.: AERONET - A federated instrument network and data archive for aerosol characterization, Rem. Sens. Environ., 66, 1-16, 1998.

Hoose, C., Kristjánsson, J. E., Iversen, T., Kirkevåg. A., Seland, Ø., and Gettelman, A.: Constraining cloud droplet number concentrations in GCMs suppresses the aerosol indirect effect, Geophys. Res. Lett., 36, L12807, doi:10.1029/2009GL038568, 2009.

Hu, L., Keller, C. A., Long, M. S., Sherwen, T., Auer, B., Da Silva, A., Nielsen, J. E., Pawson, S., Thompson, M. A., Trayanov, A. L., Travis, K. R., Grange, S. K., Evans, M. J., and Jacob, D. J.: Global simulation of tropospheric chemistry at 12.5 km resolution: performance and evaluation of the GEOS-Chem chemical module (v10-1) within the NASA GEOS Earth system model (GEOS-5 ESM), Geosci. Model Dev., 11, 4603-4620, doi:10.5194/gmd-11-4603-2018, 2018.

Huang, L., Gong, S. L., Jia, C. Q., and Lavoué, D.: Importance of deposition processes in simulating the seasonality of the Arctic black carbon aerosol. *J. Geophys. Res.* **115,** D17207, doi:10.1029/2009JD013478, 2010

Huneeus, N., Schulz, M., Balkanski, Y., Griesfeller, J., Prospero, J., Kinne, S., Bauer, S., Boucher, O., Chin, M., Dentener, F., Diehl, T., Easter, R., Fillmore, D., Ghan, S., Ginoux, P., Grini, A., Horowitz, L., Koch, D., Krol, M. C., Landing, W., Liu, X., Mahowald, N., Miller, R., Morcrette, J.-J., Myhre, G., Penner, J., Perlwitz, J., Stier, P., Takemura, T., and Zender, C. S.: Global dust model intercomparison in AeroCom phase I, Atmos. Chem. Phys., 11, 7781-7816, doi:10.5194/acp-11/7781-2011, 2011.

Ikeda, K., Tanimoto, H., Sugita, T., Akiyoshi, H., Kanaya, Y., Zhu, C., and Taketani, F.: Tagged tracer simulations of black carbon in the Arctic: transport, source contributions, and budget. Atmos. Chem. Phys., 17, 10515-10533, doi:10.5194/acp-17-10515-2017, 2017.

Ishijima, K., Takigawa, M., Yamashita, Y., Yashiro, H., Kodama, C., Satoh, M., Tsuboi, K., Matsueda, H., Niwa, Y., and Hirao, S.: Analysis of High Radon-222 Concentration Events Using Multi-Horizontal-Resolution NICAM Simulations, SOLA, 14, 111-115, doi:10.2151/sola.2018-019, 2018

https://doi.org/10.5194/gmd-2020-34
Preprint. Discussion started: 26 February 2020

Jacob, D. J., Crawford, J. H., Maring, H., Clarke, A. D., Dibb, J. E., Emmons, L. K., Ferrare, R. A., Hostetler, C. A., Russell, P. B., Singh, H. B., Thompson, A. M., Shaw, G. E., McCauley, E., Pederson, J. R., and Fisher, J. A.: The Arctic Research of the Composition of the Troposphere from Aircraft and Satellites (ARCTAS) mission: design, execution, and first results, Atmos. Chem. Phys., 10, 5191-5212, doi:10.5194/acp-10-5191-2010, 2010.

Jacobson, M. Z., Global direct radiative forcing due to multicomponent anthropogenic and natural aerosols, J. Geophys. Res., 106, D2, 1551-1568, 2001.

Janssens-Maenhout, G., Crippa, M., Guizzardi, D., Dentener, F., Muntean, M., Pouliot, G., Keating, T., Zhang, Q., Kurokawa, J., Wankmüller, R., Denier van der Gon, H., Kuenen, J. J. P., Klimont, Z., Frost, G., Darras, S., Koffi, B., and Li, M.: HTAP_v2.2: a mosaic of regional and global emission grid maps for 2008 and 2010 to study hemispheric transport of air pollution. Atmos. Chem. Phys. 15, 11411–11432, 2015.

Jing, X.W., Suzuki, K., Guo, H., Goto, D., Ogura, T., Koshiro, T., and Mümlmenstädt, J.: A multi-model study on warm precipitation biases in global models compared to satellite observations, J. Geophy. Res. Atmos., 122, 11806-11824, doi.10.1002/2017JD027310, 2017.

Jing, X., and K. Suzuki, 2018: The impact of process-based warm rain constraints on the aerosol indirect effect. *Geophys. Res. Lett.*, 45, 10729-10737, doi:10.1029/2018GL079956.

Kalnay, E., Kanamitsu, M., Kistler, R., Collins, W., Deaven, D., Gandin, L., Iredell, M., Saha, S., White, G., Woollen, J., Zhu, Y., Chelliah, M., Ebisuzaki, W., Higgins, W., Janowiak, J., Mo, K. C., Ropelewski, C., Wang, J., Leetmaa, A., Reynolds, R., Jeene, R., and Joseph, D.: The NCEP/NCAR 40-year reanalysis project, B. Am. Meteorol. Soc., 77(3), 437-,471 1996.

Kim, D., Chin, M., Yu, H., Diehl, T., Tan, Q., Kahn, R. A., Tsigaridis, K., Bauer, S. E., Takemura, T., Pozzoli, L., Bellouin, N., Schulz, M., Peyridieu, S., Chédin, A., and Koffi, B.: Sources, sinks, and transatlantic transport of North African dust aerosol: A multimodel analysis and comparison with remote sensing data, J. Geophys. Res. Atmos., 119, 6259-6277, doi:10.1002/2013JD021099, 2014.

Kinne, S.: Aerosol radiative effects with MACv2, Atmos. Chem. Phys., 19, 10919-10959, doi:10.5194/acp-19-10919-2019.

https://doi.org/10.5194/gmd-2020-34
Preprint. Discussion started: 26 February 2020

Kipling, Z., Stier, P., Johnson, C. E., Mann, G. W., Bellouin, N., Bauer, S. E., Bergman, T., Chin, M., Diehl, T., Ghan, S. J., Iversen, T., Kirkevåg, A., Kokkola, H., Liu, X., Luo, G., van Noije, T., Pringle, K. J., von Salzen, K., Schulz, M., Seland, Ø., Skeie, R. B., Takemura, T., Tsigaridis, K., and Zhang, K.: What controls the vertical distribution of aerosol? Relationships between process sensitivity in HadGEM3-UKCA and inter-model variation from AeroCom Phase II, Atmos. Chem. Phys., 16, 2221-2241, doi:10.5194/acp-16-2221-2016, 2016.

Koch, D., Schulz, M., Kinne, S., McNaughton, C., Spackman, J. R., Balkanski, Y., Bauer, S., Berntsen, T., Bond, T. C., Boucher, O., Chin, M., Clarke, A., De Luca, N., Dentener, F., Diehl, T., Dubovik, O., Easter, R., Fahey, D. W., Feichter, J., Fillmore, D., Freitag, S., Ghan, S., Ginoux, P., Gong, S., Horowitz, L., Iversen, T., Kirkevag, A., Klimont, Z., Kondo, Y., Krol, M., Liu, X., Miller, R., Montanaro, V., Moteki, N., Myhre, G., Penner, J. E., Perlwitz, J., Pitari, G., Reddy, S., Sahu, L., Sakamoto, H., Schuster, G., Schwarz, J. P., Seland, Ø., Stier, P., Takegawa, N., Takemura, T., Textor, C., van Aardenne, J. A., and Zhao, Y.: Evaluation of black carbon estimations in global aerosol models, Atmos. Chem. Phys., 9, 9001-9026, doi:10.5194/acp-9-9001-2009, 2009.

Kodama, C. Yamada, Y., Noda, A. T., Kajikawa, Y., Nasuno, T., Yamaura, T., Takahashi, H. G., Hara, M., Kawatani, Y., Satoh, M., and Sugi, M.: A 20-year climatology of a NICAM AMIP-type simulation. J. Meteorol. Soc. Japan. Ser. II 93, 393-424, doi:10.2151/jmsj.2015-024, 2015.

Koffi, B., Schulz, M., Bréon, F. -M., Dentener, F., Steensen, B. M., Griesfeller, J., Winker, D., Balkanski, Y., Bauer, S. E., Chin, M., Diehl, T., Easter, R., Ghan, S., Hauglustaine, D. A., Iversen T., Kirkevåg, A., Liu, X., Lohmann, U., Myhre, G., Rasch, P., Seland, Ø., Skeie, R. B., Steenrod, S. D., Stier, P., Tackett, J., Takemura, T., Tsigaridis, K., Vuolo, M. R., Yoon, J., and Zhang, K.: Evaluation of the aerosol vertical distribution in global aerosol models through comparison against CALIOP measurements: AeroCom phase II results, J. Geophys. Res. Atmos., 121, 7254-7283, doi:10.1002.2015JD024639, 2016.

Korras-Carraca, M. B., Pappas, V., Hatzianastassiou, N., Vardavas, I., and Matsoukas, C.: Global vertically resolved aerosol direct radiation effect from three years of CALIOP data using the FORTH radiation transfer model, Atmos. Res., 224, 138-156, doi:10.1016/j.atmosres.2019.03.024, 2019.

https://doi.org/10.5194/gmd-2020-34
Preprint. Discussion started: 26 February 2020


Geoscientific Model Development Discussions

Lauer, A., and Hamilton, K.: Simulating clouds with global climate models: A comparison of CMIP5 results with CMIP3 and satellite data, J. Clim., doi:10.1175/jcli-d-12-00451.1, 2013

Le Treut, H., and Li, Z.-X.: Sensitivity of an atmospheric general circulation model to prescribed SST changes: Feedback effects associated with the simulation of cloud optical properties, Clim. Dym., 5, 175-187, 1991.

Li, Z.,Lau, W. K.-M., Ramanathan, V., Wu, G., Ding, Y., Manoj, M. G., Liu, J., Qian, Y., Li, J., Zhou, T., Fan, J., Rosenfeld, D., Ming, Y., Wang, Y., Huang, J., Wang, B., Xu, X., Lee, S. -S., Cribb, M., Zhang, F., Yang, X., Zhao, C., Takemura, T., Wang, K., Xia, X., Yin, Y., Zhang, H., Guo, J., Zhao, P. M., Sugimoto, N., Babu, S. S, and Brasseur, G. P.: Aerosol and monsoon climate interactions over Asia, Rev. Geophy., 54, 866-929, doi:10.1002/2015RG00500, 2016

Lin, G., Qian, Y., Yan, H., Zhao, C., Ghan, S. J., Easter, R., and Zhang, K.: Quantification of marine aerosol subgrid variability and its correlation with clouds based on high-resolution regional modeling, J. Geophys. Res. Atmos., 112, 6329-6346, doi:10.1002/2017JD026567, 2017.

Liu, X., Penner, J. E., Das, B., Bergmann, D., Rodriguez, J. M., Strahan, S., Wang, M., and Feng, T.: Uncertainties in global aerosol simulations: Assessment using three meteorological data sets, J. Geophys. Res., 112, D11212, doi:10.1029/2006JD008216, 2007.

Liu, J., Fan, S., Horowitz, L. W., and Levy II, H.: Evaluation of factors controlling long-range transport of black carbon to the Arctic. J. Geophy. Res., 116, D04307, doiL10.1029/2010JD015145, 2011.

Loeb, N. G., B. A. Wielicki, D. R. Doelling, G. L. Smith, D. F. Keyes, S. Kato, N. Manalo- Smith, T. Wong: Toward optimal closure of the Earth's top-of-atmosphere radiation budget. J. Clim., **22**, 748-766, doi:10.1175/2008JCLI2637.1., 2009.

Loeb, N. G., Wielicki, B. A., Wong, T., and Parker, P. A.: Impact of data gaps on satellite broadband radiation records, J., Geophys. Res., 114, D11109, doiL10.1029/2008JD011183, 2009.

Lohmann, U., Feichter, J., Chuang, C. C., and Penner, J. E.: Prediction of the number of cloud droplets in the ECHAM GCM, J. Geophys. Res., 104 (D8), 9169-9198, 1999.

Lund, M. T., and Berntsen, T., Parameterization of black carbon aging in the OsloCTM2 and implications for regional transport to the Arctic, Atmos. Chem. Phys., 12, 6999-7014, doi:10.5194/acp-12-6999-2012, 2012.

https://doi.org/10.5194/gmd-2020-34
Preprint. Discussion started: 26 February 2020

Lund, M. T., Samset, B. H., Skeie, R. B., Watson-Parris, D., Katich, J. M., Schwarz, J. P., and Weinzierl, B.: Short black carbon lifetime from a global set of aircraft observations, npj, Clim. Sci., 1:31, doi:10.1038/s41612-018-0040-x, 2018.

Ma, P.-L., Rasch, P. J., Fast, J. D., Easter, R. C., Gustafson Jr., W. I., Liu, X., Ghan S. J., and Singh, S.: Assessing the CAM5 physics suite in the WRF-Chem model: implementation, resolution sensitivity, and a first evaluation for regional case study, Geosci. Model Dev., 7, 755-778, doi:10.5194/gmd-7-755-2014, 2014.

Malavell, F. F., Haywood, J. M., Jones, A., Gettelman, A., Clarisse, L., Bauduin, S., Allan R. P., Karset, I. H. H., Krisjánsson, J. E., Oreopoulos, L., Cho, N., Lee, D., Bellouin, N., Boucher, O., Grosvenor, D. P., Carslaw, K. S., Dhomse, S., Mann, G. W., Schmidt, A., Coe, H., Hartley, M. E., Dalvi, M., Hill, A. A., Johnson, B. T., Johnson, C. E., Knight, J. R., O'Connor, F. M., Partridge, D. G., Stier, P., Myhre, G., Platnick, S., Stephens, G. L., Takahashi, H., and Thordarson, T.: Strong constraints on aerosol-cloud interactions from volcanic eruptions, Nature, 546, 485-491, doi:10.1038/nature22974, 2017.

Marelle, L., Raut, J. -C., Law, K. S., Berg, L. K., Fast, J. D., Easter, R. C., Shrivastava, M., and Thomas, J. L.: Improvements to the WRF-Chem 3.5.1 model for quasi-hemispheric simulations of aerosols and ozone in the Arctic, Geosci. Model Dev., 10, 3661-3677, doi:10.5194/gmd-3661-2017, 2017.

Matsui, H., Kondo, Y., Moteki, N., Takegawa, N., Sahu, L. K., Zhao, Y., Fuelberg, H. E., Sessions, W. R., Diskin, G., Blake, D. R., Wisthaler, A., and Koike, M.: Seasonal variation of the transport of black carbon aerosol from the Asian continent to the Arctic during the ARCTAS aircraft campaign, J. Geophys. Res., 115, D05202, doi:10.1029/2010JD015067, 2011.

Matsui, H., and Mahowald, N.: Development of a global aerosol model using a two-dimensional sectional method: 2. Evaluation and sensitivity simulations. J. Adv. Model. Earth Syst., 9, 1887-1920, doi:10.1002/2017MS000937, 2017.

Mellor, G. L., and Yamada, T.: A hierarchy of turbulence closure models for planetary boundary layers, J. Atmos. Sci., 31, 1791–1806, doi: 10.1175/1520-0469(1974)031<1791:AHOTCM>2.0.CO;2, 1974.

Miura, H.: An upwind-biases conservative advection scheme for spherical hexagonal-pentagonal grids, Mon. Wea. Rev., 135, 4038-4044, 2007.

Miyamoto, Y., Kajikawa, Y., Yoshida, R., Yamaura, T., Yashiro, H., and Tomita, H.: Deep moist atmospheric convection in a subkilometer global simulation, Geophys. Res. Lett., 40(18), 4922-4926, doi:10.1002/grl.50944, 2013.

https://doi.org/10.5194/gmd-2020-34
Preprint. Discussion started: 26 February 2020

Monahan, E. C., Spiel, D. E., and Davidson, K. L.: A model of marine aerosol generation via whitecaps and wave disruption, in Oceanic Whitecaps and Their Role in Air-Sea Exchange Processes, edited by E. C. Monahan and G. M. Niocaill, pp. 167-174, Springer, New York, 1986.

Myhre G., Samset, B.H., Schulz, M., Balkanski, Y., Bauer, S., Berntsen, T.K., Bian, H., Bellouin, N., Chin, M., Diehl, T., Easter, R.C., Feichter, J., Ghan, S.J., Hauglustaine, D., Iversen, T., Kinne, S., Kirkevåg, A., Lamarque, J.-F., Lin, G., Liu, X., Lund, M.T., Luo, G., Ma, X., van Noije, T., Penner, J.E., Rasch, P.J., Ruiz, A., Seland, Ø., Skeie, R.B., Stier, P., Takemura, T., Tsigaridis, K., Wang, P., Wang, Z., Xu, L., Yu, H., Yu, F., Yoon, J.-H., Zhang, K., Zhang, H., and Zhou, C.: Radiative forcing of the direct aerosol effect from AeroCom Phase II simulations, Atmos. Chem. Phys. 13, 1853-1877. doi:10.5184/acp-13-1853-2013, 2013.

Nakajima, T., Tonna, G., Rao, R., Kaufman, Y., and Holben, B.: Use of sky brightness measurements from ground for remote sensing of particulate polydispersions. Appl. Optics, 35, 2672–2686, 1996.

Nakanishi, M., and Niino, H.: An improved Mellor–Yamada level 3 model with condensation physics: its design and verification, Bound. Layer Meteor., 112, 1–31, doi:10.1023/B:BOUN.0000020164.04146.98, 2004.

Nam, C., Bony S., Dufresne, J.-L., and Chepfer, H.: The 'too few, too bright' tropical low-cloud problem in CMIP5 models, Geophy. Res. Lett., 39, L21801, doi:10.1029/2012GL053421, 2012.

Niwa, Y., Tomita, H., Satoh, M., and Imasu, R.: A three-dimensional icosahedral grid advection scheme preserving monotonicity and consistency with continuity for atmospheric tracer transport, J. Meteor. Soc. Jpn, 89, 255–268, doi: 10.2151/jmsj.2011-306, 2011.

Ohmura, A., Dutton, E.G., Forgan, B., Fröhlich, C., Gilgen, H., Hegner, H., Heimo, A., König-Langlo, G., McArthur, B., Müller, G., Philipona, R., Pinker, R., Whitlock, C.H., Dehne, K., and Wild, M.: Baseline surface radiation network (BSRN/WCRP), a new precision radiometry for climate research. B. Am. Meteorol. Soc., 79, 2115-2136, 1998.

Oikawa, E., Nakajima, T., and Winker, D.: An evaluation of the shortwave direct aerosol radiative forcing using CALIOP and MODIS observations, J. Geophys. Res., 123, 1211-1233, doi:10.1029/2017JD027247, 2018.

https://doi.org/10.5194/gmd-2020-34
Preprint. Discussion started: 26 February 2020

Oshima, N., Kondo, Y., Moteki, N., Takegawa, N., Koike, M., Kita, K., Matsui, H., Kajino, M., Nakamura, H., Jung, J. S., and Kim, Y. J.: Wet removal of black carbon in Asian outflow: Aerosol Radiative Forcing in East Asia (A-FORCE) aircraft campaign, J. Geophys. Res., 117, D3204, doi:10.1029/2011JD016552, 2012.

Partanen, A. -I., Dunne, E. M., Bergman, T., Laakso, A., Kokkoka, H., Ovadnevaite, J., Sogacheva, L., Baisnée, D., Sciare, J., Manders, A., O'Dowd, C., de Leeuw, G., and Korhonen, H.: Global modelling of direct and indirect effects of sea spray aerosol using a source function encapsulating wave state, Atmos. Chem. Phys., 14, 11731-11752, doi:10.5194/acp-14-11731-2014, 2014.

Pincus, R., McFarlane, S. A., and Klein, S. A.: Albedo bias and the horizontal variability of clouds in subtropical marine boundary layers: Observations from ships and satellites, J. Geophys. Res., 104, D6, 6183-6191, 1999.

Platnick, S., et al., 2015. MODIS Atmosphere L3 Monthly Product. NASA MODIS Adaptive Processing System, Goddard Space Flight Center, USA: http://dx.doi.org/10.5067/MODIS/MOD08_M3.006

Prospero, J. M., Uematsu, M., and Savoie, D.: Mineral aerosol transport to the Pacific Ocean, in Chemical Oceanography, edited by Riley, J. P., Chester, R., and Duce, R. A., 10, 188–218, Academic, New York, USA, 1989.

Qian, Y., Gustafson Jr., W. I., and Fast, J. D.: An investigation of the sub-grid variability of trace gases and aerosols for global climate modeling, Atmos. Chem. Phys., 10, 6917-6946, doi:10.5194/acp-10-6917-2010, 2010

Quinn, P. K., Stohl, A., Arneth, A., Berntsen, T., Burkhart, J., Christensen, J., Flanner, M., Kupiainen, K., Luhavainen, H., Shepherd, M., Shevchenko, V., Skov, H., and Vestreng, V.: The Impact of black carton on Arctic climate, 4, Arctic Monitoring and Assessment Progrramme (AMAP), 2011.

Raut, J. -C., Marelle, L., Fast, J. D., Thomas, J. L., Weinzierl, B., Law, K. S., Berg, L. K., Roiger, A., Easter, R. C., Heimerl, K., Onishi, T., Delanoë, and Schlager, H.: Cross-polar transport and scavenging of Siberian aerosols containing black carbon during the 2012 ACCESS summer campaign, Atmos. Chem. Phys., 17, 10969-10995, doi:10.5194/acp-17-10969-2017, 2017.

Samset, B. H., Myhre, G., Schulz, M., Balkanski, Y., Bauer, S., Berntsen, T. K., Bian, H., Bellouin, N., Diehl, T., Easter, R. C., GHan, S. J., Iversen, T., Kinne, S., Kirkevåg, A., Lamarque, J.-F., Lin, G., Liu, X., Penner, J. E., Seland, Ø., Skeie, R. B.,

https://doi.org/10.5194/gmd-2020-34
Preprint. Discussion started: 26 February 2020

Stier, P., Takemura, T., Tsigaridis, K., and Zhang, K.: Black carbon vertical profiles strongly affect its radiative forcing uncertainty, Atmos. Chem. Phys., 13, 2423-2434, doi:10.5194-acp-13-2423-2013, 2013.

Sand, M., Samset, B., Balkanski, Y., Bauer, S., Bellouin, N., Berntsen, T. K., Bian, H., Chin, M., Diehl, T., Easter, R., Ghan, S. J., Iversen, T., Kirkevåg, A., Lamarque, J. -F., Lin, G., Liu, X., Luo, G., Myhre,G., van Noije, T., Penner, J. E., Schulz, M., Seland, Ø., Skeie, R. B., Stier, P., Takemura, T., Tsigaridis, K., Yu, F., Zhang, K., and Zhang, H.: Aerosols at the poles: an AeroCom Phase II multi-model evaluation, Atmos. Chem. Phys., 17, 12197-12218, doi:10.5194/acp-17-12197-2017, 2017.

Sato, Y., Goto, D., Michibata, T., Suzuki, K., Takemura, T., Tomita, H., and Nakajima, T.: Aerosol effects on cloud water amounts were successfully simulated by a global cloud-system resolving model, Nature Com., 9: 985, doi:10.1038/s41467-018-03379-6, 2018.

Sato, Y., Miura, H., Yashiro, H., Goto, D., Takemura, T., Tomita, H., and Nakajima, T.: Unrealistically pristine air in the Arctic produced by current global scale models, Sci. Rep., 6, 26561, doi:10.1038/resp26561, 2016.

Sato, Y., and Suzuki, K.: How do aerosols affect cloudiness?, Science, 363, 580-581, doi:10.1126/science.aaw3720, 2019.

Satoh, M., Matsuno, T., Tomita, H., Miura, H., Nasuno, T., and Iga, S.: Nonhydrostatic icosahedral atmospheric model (NICAM) for global cloud resolving simulations. J. Comput. Phys., 227, 3486-3514. doi:10.1016/j.jcp.2007.02.006, 2008.

Satoh, M., Inoue, T., and Miura, H.: Evaluations of cloud properties of global and local cloud system resolving models using CALIPSO and CloudSat simulators, J. Geophys. Res., 115, D00H14, doi:10.1029/2009JD012247, 2010.

Satoh, M., Tomita, H., Yashiro, H., Miura, H., Kodama, C., Seiki, T., Noda, A.T., Yamada, Y., Goto, D., Sawada, M., Miyoshi, T., Niwa, Y., Hara, M., Ohno, T., Iga, S., Arakawa, T., Inoue, T., and Kubokawa, H.: The non-hydrostatic icosahedral atmospheric model: description and development. Progress in Earth and Planetary Science 1, 18-49. doi:10.1186/s40645-014-0018-1, 2014.

Schwarz, J. P., Gao, R. S., Fahey, D. W., Thomson, D. S., Watts, L. A., Wilson, J. C., Reeves, J. M., Darbeheshti, M., Baumgardner, D. G., Kok, G. L., Chung, S. H., Schulz, M., Hendricks, J., Lauer, A., Kärcher, B., Slowik, J. G., Rosenlof, K. H., Thompson, T. L., Langford, A. O., Loewenstein, M., and Aikin, K. C.: Single-particle measurements

https://doi.org/10.5194/gmd-2020-34
Preprint. Discussion started: 26 February 2020

of midlatitude black carbon and light-scatting aerosols from the boundary layer to the lower stratosphere, J. Geophys. Res., 111, D16207, doi:10.1029/2006JD007076, 2006.

Schwarz, J. P., Spackman, J. R., Gao, R. S., Watts, L. A., Stier, P., Schulz, M., Davis, S. M., Wofsy, S. C., and Fahey, D. W.: Global-scale black carbon profiles observed in the remote atmosphere and compared to models, Geophys. Res. Lett., 37, L18812, doi:10.1029/2010GL044372, 2010.

Schwarz, J. P., Samset, B. H., Perring, A. E., Spackman, J. R., Gao, R. S., Stier, P., Schulz, M., Moore, F. L., Ray, E. A., and Fahey, D. W.: Global-scale seasonally resolved black carbon vertical profiles over the Pacific, Geophys. Res. Lett., 40, 5542-5547, doi:10.1002/2013GL057775, 2013.

Schutgens, N. A. J., Gryspeerdt, E., Weigum, N., Tsyro, S., Goto, D., Schulz, M., and Stier, P.: Will a perfect model agree with perfect observations? The impact of spatial sampling. Atmos. Chem. Phys., 16, 6335-6353, doi:10.5194/acp-16-6335-2016, 2016

Sekiguchi, M., and Nakaima, T.: A k-distribution-based radiation code and its computational optimization for an atmospheric general circulation model, J. Quant. Spectrosc. Radiat. Transf., 109, 2779-2793, doi: 10.1016/j.jqsrt.2008.07.013, 2008.

Sekiya, T., Miyazaki, K., Ogochi, K., Sudo, K., and Takigawa, M.: Global high-resolution simulations of tropospheric nitrogen dioxide using CHASER V4.0, Geosci. Model Dev., 11, 958-988, doi:10.5194/gmd-11-959-2018, 2018.

Sharma, S., Leaitch, W. R., Huang, L., Veber, D., Kolonjari, F., Zhang, W., Hanna, S. J., Bertram, A. K., and Ogren, J. A.: An evaluation of three methods for measuring black carbon in Alert, Canada, Atmos. Chem. Phys., 17, 15255-15243, doi:10.5194/acp-17-15225-2017, 2017.

Shindell, D.T., Chin, M., Dentener, F., Doherty, R. M., Faluvegi, G., Fiore, A. M., Hess, P., Koch, D. M., MacKenzie, I. A., Sanderson, M. G., Schultz, M. G., Schulz, M., Stevenson, D. S., Teich, H., Textor, C., Wild, O., Bergmann, D. J., Bey, I., Bian, H., Cuvelier, C., Duncan, B. N., Folberth, G., Horowitz, L. W., Jonson, J., Kaminski, J. W., Marmer, E., Park, R., Pringle, K. J., Schroeder, S., Szopa, S., Takemura, T., Zeng, G., Keating, T. J., and Zuber, A.: A multi-model assessment of pollution transport to the Arctic, Atmos. Chem. Phys., 8, 5353-5372, doi: 10.5194/acp-8-5353-2008, 2008

https://doi.org/10.5194/gmd-2020-34
Preprint. Discussion started: 26 February 2020

Sinha, P. R., Kondo, Y., Koike, M., Ogren, J. A., Jefferson, A., Barrett, T. E., Sheesley, R. J., Ohara, S., Moteki, N., Coe, H., Liu, D., Irwin, M., Tunved, P., Quinn, P. K., and Zhao, Y.: Evaluation of ground-based black carbon measurements by filter-based photometers at two Arctic sites, J. Geophys. Res. Atmos., 122, 3544-3572, doi:10.1002/2016JD025843, 2017.

Stevens, B., and Feingold, G.: Untangling aerosol effects on clouds and precipitation in a bufferred system, Nature, 461, 607-613, doi:10.1038/nature08281, 2009.

Su, W., Loeb, N. G., Schuster, G. L., Chin, M., and Rose, F. G.: Global all-sky shortwave direct radiative forcing of anthropogenic aerosols from combined satellite observations and GOCART simulations: J. Geophys. Res. Atmos. 118, 655-669, doi:10.1029/2012JD018294, 2013.

Sudo, K., Takahashi, M., Kurokawa, J., and Akimoto, H.: CHASER: A global chemical model of the troposphere: 1. Model description, J. Geophy. Res., 107 (D17), 4339, doi:10.1029/2001JD001113, 2002.

Suzuki, K., Nakajima, T., Satoh, M., Tomita, H., Takemura, T., Nakajima, T.Y., and Stephens, G.L.: Global cloud-system-resolving simulation of aerosol effect on warm clouds. Geophy. Res. Lett., 35, L19817. doi:10.1029/2008GL035449, 2008.

Takata, K., Emori, S., and Watanabe, T.: Development of the minimal advanced treatments of surface interaction and runoff, Global. Planet. Change, 38, 209-222, doi: 10.1016/S0921-8181(03)00030-4, 2003.

Takemura, T., Okamoto, H., Maruyama, Y., Numaguti, A., Higurashi, A., and T. Nakajima, T.: Global three-dimensional simulation of aerosol optical thickness distribution of various origins, J. Geophys. Res., 105, 17853–17873, doi: 10.1029/2000JD900265, 2000.

Takemura, T., Nozawa, T., Emori, S., Nakajima, T.Y., and Nakajima, T.: Simulation of climate response to aerosol direct and indirect effects with aerosol transport-radiation model. J. Geophy. Res., 110, D02202, doi:10.1029/2004JD005029, 2005.

Textor, C., Schulz, M., Guibert, S., Kinne, S., Balkanski, Y., Bauer, S., Berntsen, T., Berglen, T., Boucher, O., Chin, M., Dentener, F., Diehl, T., Easter, R., Feichter, J., Fillmore, D., Ghan, S., Ginoux, P., Gong, S., Grini, A., Hendricks, J., Horowitz, L., Huang, P., Isaksen, I., Iversen, T., Kloster, S., Koch, D., Kirkevåg, A., Kristjansson, J. E., Krol, M.,

https://doi.org/10.5194/gmd-2020-34
Preprint. Discussion started: 26 February 2020

Lauer, A., Lamarque, J. F., Liu, X., Montanaro, V., Myhre, G., Penner, J. E., Pitari, G., Reddy, S., Seland, Ø., Stier, P., Takemura, T., and Tie, X.: Analysis and quantification of the diversities of aerosol life cycles within AeroCom, Atmos. Chem. Phys., 6, 1777–1813, doi: 10.5194/acp-6-1777-2006, 2006.

Tomita, H.: New microphysics with five and six categories with diagnostic generation of cloud ice, J. Meteorol. Soc. Jpn., 86A, 121-142, 2008.

Tomita, H. and Satoh, M.: A new dynamical framework of nonhydrostatic global model using the icosahedral grid, Fluid Dyn. Res., 34, 357-400, 2004.

Tsigaridis, K., Daskalakis, N., Kanakidou, M., Adams, P. J., Artaxo, P., Bahadur, R., Balkanski, Y., Bauer, S. E., Bellouin, N., Benedetti, A., Bergman, T., Berntsen, T. K., Beukes, J. P., Bian, H., Carslaw, K. S., Chin, M., Curci, G., Diehl, T., Easter, R. C., Ghan, S. J., Gong, S. L., Hodzic, A., Hoyle, C. R., Iversen, T., Jathar, S., Jimenez, J. L., Kaiser, J. W., Kirkevåg, A., Koch, D., Kokkola, H., Lee, Y. H., Lin, G., Liu, X., Luo, G., Ma, X., Mann, G. W., Mihalopoulos, N., Morcrette, J.-J., Müller, J.-F., Myhre, G., Myriokefalitakis, S., Ng, N. L., O'Donnell, D., Penner, J. E., Pozzoli, L., Pringle, K. J., Russell, L. M., Schulz, M., Sciare, J., Seland, Ø., Shindell, D. T., Sillman, S., Skeie, R. B., Spracklen, D., Stavrakou, T., Steenrod, S. D., Takemura, T., Tiitta, P., Tilmes, S., Tost, H., van Noije, T., van Zyl, P. G., von Salzen, K., Yu, F., Wang, Z., Wang, Z., Zaveri, R. A., Zhang, H., Zhang, K., Zhang, Q., and Zhang, X.: The AeroCom evaluation and intercomparison of organic aerosol in global models, Atmos. Chem. Phys., 14, 10845-10895, doi:10.5194/acp-14-10845-2014, 2014.

van der Werf, Randerson, J. T., Giglio, L., van Leeuwen, T. T., Chen, Y., Rogers, B. M., Mu, M., van Marle, M. J. E., Morton, D. C., Collatz, G. J., Yokelson, R. J., and Kasibhatla, P. S.: Global fire emissions estimates during 1997-2016, Earth Syst. Sci. Data, 9, 697-720, doi:10.5194/essd-9-697-2017, 2017.

Vignati, E., Karl, M., Krol, M., Wilson, J., Stier, P., and Cavalli, F.: Sources of uncertainties in modelling black carbon at the global scale, Atmos. Chem. Phys., 10, 2595-2611, doi:10.5194/acp-10-2595-2010. 2010.

Watson-Parris, D., Schutgems, N. Winker, D., Burton, S. P., Ferrare, R. A., and Stier, P.: On the limits of CALIOP for constraining modeled free tropospheric aerosol. Geophys. Res. Lett., 45, 9260-9266, doi:10.1029/2018GL078195, 2018.

https://doi.org/10.5194/gmd-2020-34
Preprint. Discussion started: 26 February 2020

Willis, M. D., Leaitch, W. R., and Abbatt, J. P. D.: Processes controlling the composition and abundance of Arctic aerosol, Rev. Geophy., 56, doi:10.1029/2018RG000602, 2018.

Winker, D. M., Tackett, J. L., Getzewich, B. J., Liu, Z., Vaughan, M. A., and Rogets, R. R.: The global 3-D distribution of tropospheric aerosols as characterized by CALIOP, Atmos. Chem. Phys., 13, 3345-3361, doi:10.5194/acp-13-3345-2013, 2013.

Wofsy, S. C., B. C. Daube, R. Jimenez, E. Kort, J. V. Pittman, S. Park, R. Commane, B. Xiang, G. Santoni, D. Jacob, J. Fisher, C. Pickett-Heaps, H. Wang, K. Wecht, Q.-Q. Wang, B. B. Stephens, S. Shertz, A.S. Watt, P. Romashkin, T. Campos, J. Haggerty, W. A. Cooper, D. Rogers, S. Beaton, R. Hendershot, J. W. Elkins, D. W. Fahey, R. S. Gao, F. Moore, S. A. Montzka, J. P. Schwarz, A. E. Perring, D. Hurst, B. R. Miller, C. Sweeney, S. Oltmans, D. Nance, E. Hintsa, G. Dutton, L. A. Watts, J. R. Spackman, K. H. Rosenlof, E. A. Ray, B. Hall, M. A. Zondlo, M. Diao, R. Keeling, J. Bent, E. L. Atlas, R. Lueb, M. J. Mahoney: HIPPO Merged 10-second Meteorology, Atmospheric Chemistry, Aerosol Data (R_20121129). Carbon Dioxide Information Analysis Center, Oak Ridge National Laboratory, Oak Ridge, Tennessee, U.S.A. http://dx.doi.org/10.3334/CDIAC/hippo_010 , 2012.

Yasunari, T. J., Kim, K.-M., da Silva, A. M., Hayasaki, M., Akiyama, M., and Murao, N.: Extreme air pollution events in Hokkaido, Japan, traced back to early snowmelt and large-scale wildfires over East Eurasia: Case studies, Sci. Rep., 8, 6413, doi:10.1038/s41598-018-24335-w, 2018.

Yu, P., Froyd, K. D., Portmann, R. W., Toon, O. B., Freitas, S. R., Bardeen, C. G., Brock, C., Fan, T., Gao, R. -S., Latich, J. M., Kupc, A., Liu, S., Maloney, C., Murphy, D. M., Rosenlof, K. H., Schill, G., Schwarz, J. P., and Williamson, C.: Efficient in-cloud removal of aerosols by deep convection, Geophys. Res. Lett., 46, 1061-1069, doi:10.1029/2018GL080544, 2019.

Zhang, X. Y., Wang, Y. Q., Niu, T., Zhang, X. C., Gong, S. L., Zhang, Y. M., and Sun, J. Y.: Atmospheric aerosol compositions in China: spatial/temporal variability, chemical signature, regional haze distribution and comparisons with global aerosols, Atmos. Chem. Phys., 12, 779-799, doi: 10.5194/acp-12-779-2012, 2012.

https://doi.org/10.5194/gmd-2020-34
Preprint. Discussion started: 26 February 2020

Geoscientific Model Development Discussions

Table 1. Datasets of observation including information about period

Name	Product	Variables	Region	Period	Reference
MODIS/Terra	Satellite	Cloud optical thickness, Cloud fraction, Aerosol optical thickness (AOT)	Global (1°×1°)	2012-2014	Collection 6 for both clouds and aerosols retrieved from NASA
CALIOP/CALIPSO		Vertical extinction coefficient for aerosols	Global (1°×1°)	2012-2014	Version 3 (Winker et al., 2013)
CERES		Top-of-atmosphere radiation fluxes	Global (1°×1°)	2012-2014	CERES_EBAF_Ed2.8 provided by NASA/LaRC (Langley Research Center) Hampton
NCEP	Reanalysis	U and V (wind speed components) at a height of 10 m	Global (2.5°×2.5°)	2012-2014	NCEP/NCAR Reanalysis 1: Surface Flux
GPCP		Precipitation	Global (2.5°×2.5°)	2012-2014	Version 2.3 by Adler et al. (2003)
AERONET	In situ measurement	AOT	Global	2000-2015	Level 2 daily version 2; accessed on 2015/06/27; Holben et al. (1998)
SKYNET			Asia and New Zealand	2005-2015[#1]	Nakajima et al. (1996)
CARSNET			China	2002-2013	Che et al. (2015)
BSRN		Radiation fluxes (global, direct and diffuse) at the surface	Global	2008-2012	Ohmura et al. (1998)
IMPROVE		Aerosol mass concentration at the surface	United States	2006-2015[#1]	IMPROVE (Interagency Monitoring of Protected Visual Environments)
EMEP			Europe	2007-2015[#1]	WMO Global Atmosphere Watch, World Data Center for Aerosols
EANET			Asia	2005-2013[#1]	EANET (Acid Deposition Monitoring Network in East Asia; http://eanet.asia)
CAWNET			China	2006-2007	Zhang et al. (2012)
University of Miami, US			Global	Some in the 1980s and others after 2000	Prospero et al. (1989); Liu et al. (2007)

[#1] The period depends on the site.

https://doi.org/10.5194/gmd-2020-34
Preprint. Discussion started: 26 February 2020

Geoscientific Model Development Discussions

Table 2. Global aerosol budgets simulated by the HRM and LRM

Species	Parameter	HRM	LRM	DIF*	Reference
Dust	Column [Tg]	27.08	27.01	0	15.8 (6.8-29.5)[k],19.20 (11.5-26.9)[a], 28.5[b]
	Emission [Tg/yr]	1805	1911	6	1123 (514-4313)[k],1840 (938-2742)[a], 2677[b]
	Dry Deposition [Tg/yr]	342	363	6	396 (37-2791)[k]
	Grav. Deposition [Tg/yr]	634	663	5	314 (22-2475)[k]
	Wet Deposition [Tg/yr]	825	880	7	357 (295-1382)[k]
	Lifetime [Day]	5.49	5.17	-6	3.9[b], 4.14 (2.36-5.92)[a], 4.6 (1.6-7.1)[k]
Sea salt	Column [Tg]	5.60	5.42	-3	5.62[l], 6.8[c], 7.52 (3.5-11.6)[a], 13.6[b]
	Emission [Tg/yr]	8856	9624	9	805 (378-1233)[e], 3529[l], 4015.5[c], 5039[b],10200[d], 16600±199%[a],
	Dry Deposition [Tg/yr]	2272	2169	-5	1313[l]
	Grav. Deposition [Tg/yr]	1998	1951	-2	327[l]
	Wet Deposition [Tg/yr]	4586	5504	20	1889[l]
	Lifetime [Day]	0.23	0.21	-11	0.03-1.59[a], 0.48 (0.20-0.76)[a], 0.62[c], 0.80[l], 0.98[b]
Sulfate	Column [TgS]	0.38	0.32	-16	0.59 (0.34-0.93)[j], 0.66 (0.50-0.83)[a]
	Production [TgS/yr]	58.4	56.7	-3	37.6-61.1[l] ,44.0[b]
	Dry Deposition [TgS/yr]	3.9	3.6	-8	5.8-7.6[l]
	Grav. Deposition [Tg/yr]	0.5	0.4	-8	0.0[l]
	Wet Deposition [TgS/yr]	52.0	50.4	-3	31.8-53.5[l]
	Lifetime [Day]	2.38	2.05	-14	3.3[b], 4.12 (3.4-4.9)[a]
POM	Column [Tg]	1.04	0.94	-10	1.2[m], 1.6 (0.8-2.6)[i] ,1.70 (1.24-2.16)[a],
	Emission [Tg/yr]	82.2	81.9	0	96.6 (71.5-121.7)[a]
	Dry Deposition [Tg/yr]	6.3	6.6	4	approximately 15 (0.2-28)[i]
	Grav. Deposition [Tg/yr]	3.7	3.9	5	
	Wet Deposition [Tg/yr]	72.6	71.4	-2	approximately 90 (approximately 50-140)[i]
	Lifetime [Day]	4.60	4.17	-9	5.3[m], approximately 6 (approximately 4-8)[i] ,6.54 (4.77-8.31)[a]
BC	Column [Tg]	0.13	0.10	-23	0.11[b] ,0.22[m], 0.24 (0.14-0.34)[a]
	Emission [Tg/yr]	7.3	7.3	-1	11.9 (9.2-14.6)[a]
	Dry Deposition [Tg/yr]	0.8	0.8	-1	
	Grav. Deposition [Tg/yr]	0.2	0.2	1	
	Wet Deposition [Tg/yr]	6.3	6.3	-1	
	Lifetime [Day]	6.37	4.96	-22	<5 [f,g], 5.0[b], 6.4[m], 7.12 (4.77-9.47)[a], 7.4[h]
WSBC	Column [Tg]	0.06	0.05	-11	0.19[m]
	Emission [Tg/yr]	4.5	4.5	-1	

https://doi.org/10.5194/gmd-2020-34
Preprint. Discussion started: 26 February 2020

Geoscientific Model Development Discussions

	Dry Deposition [Tg/yr]	0.4	0.4	3	
	Grav. Deposition [Tg/yr]	0.2	0.2	1	
	Wet Deposition [Tg/yr]	3.9	3.9	-1	
	Lifetime [Day]	4.78	4.29	-10	6.4[m]
WIBC	Column [Tg]	0.07	0.05	-33	0.03[m]
	Emission [Tg/yr]	2.8	2.8	-1	
	Dry Deposition [Tg/yr]	0.4	0.4	-4	
	Grav. Deposition [Tg/yr]	0.0	0.0	-6	
	Wet Deposition [Tg/yr]	2.4	2.4	0	
	Lifetime [Day]	8.95	6.04	-33	1.0[m], 1.0-1.7[n], 9.6 (w/o aging)[n]

* DIF is defined as (LRM-HRM)/HRM in percent.

[a] Textor et al. (2006); [b] Matsui and Mahowald (2017); [c] Bian et al. (2019); [d] Grythe et al. (2014); [e] Partanen et al. (2014); [f] Lund et al. (2018); [g] Samset et al. (2014); [h] Shindell et al. (2008); [i] Tsigaridis et al. (2014); [j] Myhre et al. (2013); [k]Huneeus et al. (2011); [l]Takemura et al. (2000); [m] Chung and Seinfeld (2002); [n] Goto et al. (2012)

5

https://doi.org/10.5194/gmd-2020-34
Preprint. Discussion started: 26 February 2020

Geoscientific Model Development Discussions

Table 3. Direct ARFs* at the TOA and the surface in units of W m^{-2}

Wavelength	Species	TOA				Surface			
		All-sky		Clear-sky		All-sky		Clear-sky	
		HRM	LRM	HRM	LRM	HRM	LRM	HRM	LRM
SW+LW	Dust	-0.71	-0.72	-0.92	-0.95	-1.17	-1.22	-1.36	-1.41
	Sea salt	-0.48	-0.47	-0.74	-0.75	-0.29	-0.31	-0.29	-0.30
	Sulfate	-0.45	-0.39	-0.67	-0.61	-0.38	-0.33	-0.57	-0.51
	intBC+POM	0.05	0.06	0.01	0.01	-0.36	-0.33	-0.41	-0.39
	SOA	-0.23	-0.21	-0.34	-0.31	-0.32	-0.29	-0.42	-0.39
	extBC (WIBC)	0.09	0.07	0.05	0.05	-0.21	-0.14	-0.25	-0.17
	All	-1.73	-1.67	-2.60	-2.57	-2.74	-2.63	-3.30	-3.18
SW	Dust	-0.85	-0.87	-1.10	-1.13	-1.47	-1.55	-1.69	-1.79
	Sea salt	-0.52	-0.52	-0.85	-0.88	-0.54	-0.53	-0.86	-0.89
	Sulfate	-0.47	-0.41	-0.71	-0.64	-0.46	-0.40	-0.68	-0.61
	intBC+POM	0.05	0.05	0.01	0.01	-0.37	-0.34	-0.43	-0.40
	SOA	-0.23	-0.21	-0.34	-0.32	-0.33	-0.30	-0.44	-0.41
	extBC (WIBC)	0.09	0.06	0.05	0.04	-0.21	-0.15	-0.25	-0.17
	All	-1.95	-1.89	-2.95	-2.93	-3.37	-3.27	-4.36	-4.28

* The estimated ARFs are 1-year averages due to the limited computer resource.

https://doi.org/10.5194/gmd-2020-34
Preprint. Discussion started: 26 February 2020

Geoscientific Model Development
Discussions
Open Access
EGU

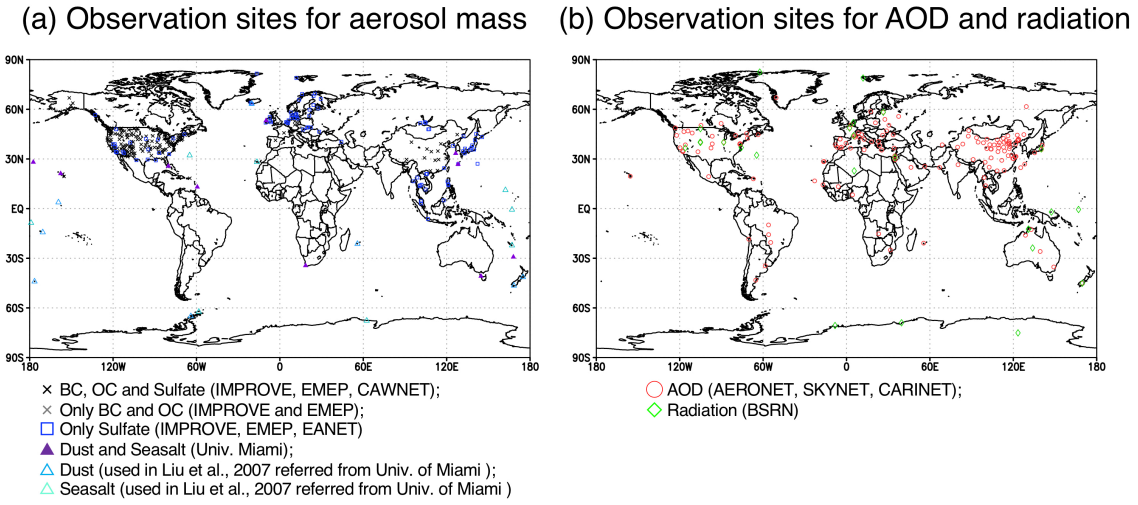

Figure 1: Global distribution of observation sites used in the model evaluation. Detailed information on these sites is provided in the supplementary material.

5

https://doi.org/10.5194/gmd-2020-34
Preprint. Discussion started: 26 February 2020

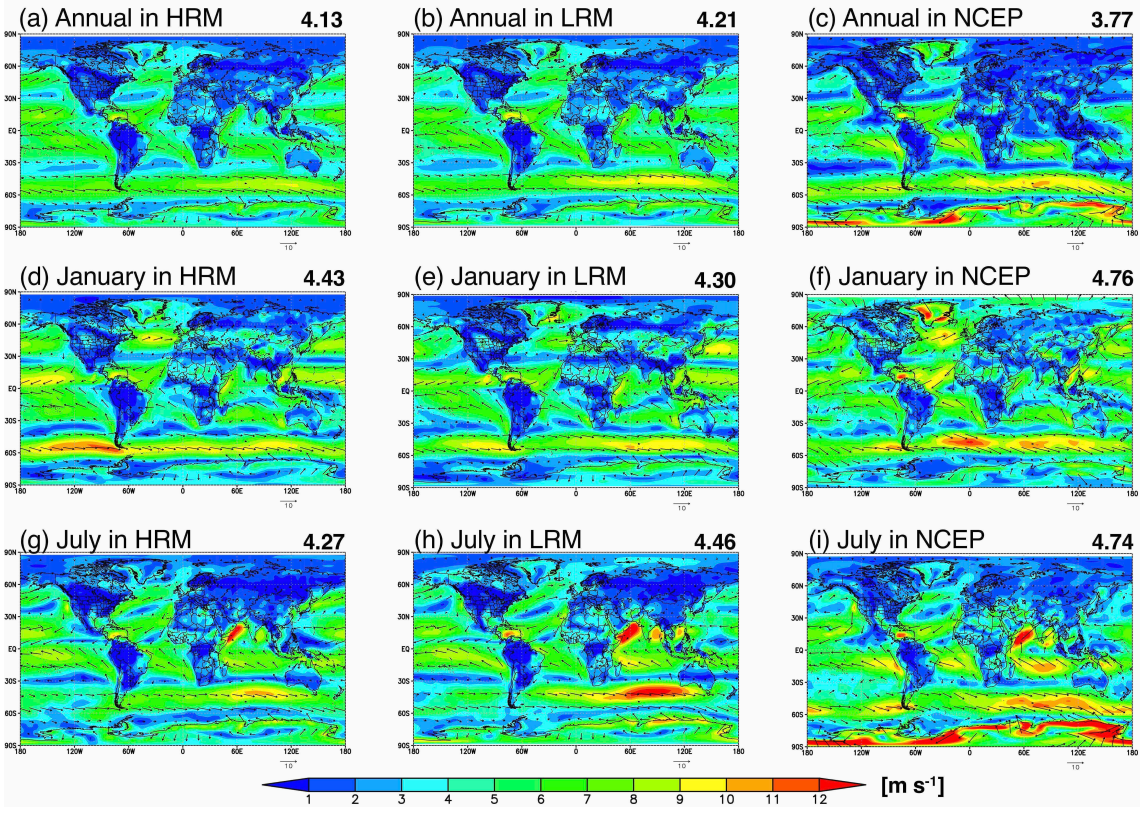

Figure 2: Global distributions of the annual, January and July averages of the wind speed at a height of 10 m simulated by the HRM and LRM and reanalyzed by the NCEP. The colors and arrows represent the wind speed and wind direction, respectively. The model results in both the HRM and the LRM are horizontally interpolated onto the NCEP grids (2.5°×2.5°). The numbers shown in the upper-right corner in each panel represent the global averages. All units are in m s^{-1}.

https://doi.org/10.5194/gmd-2020-34
Preprint. Discussion started: 26 February 2020

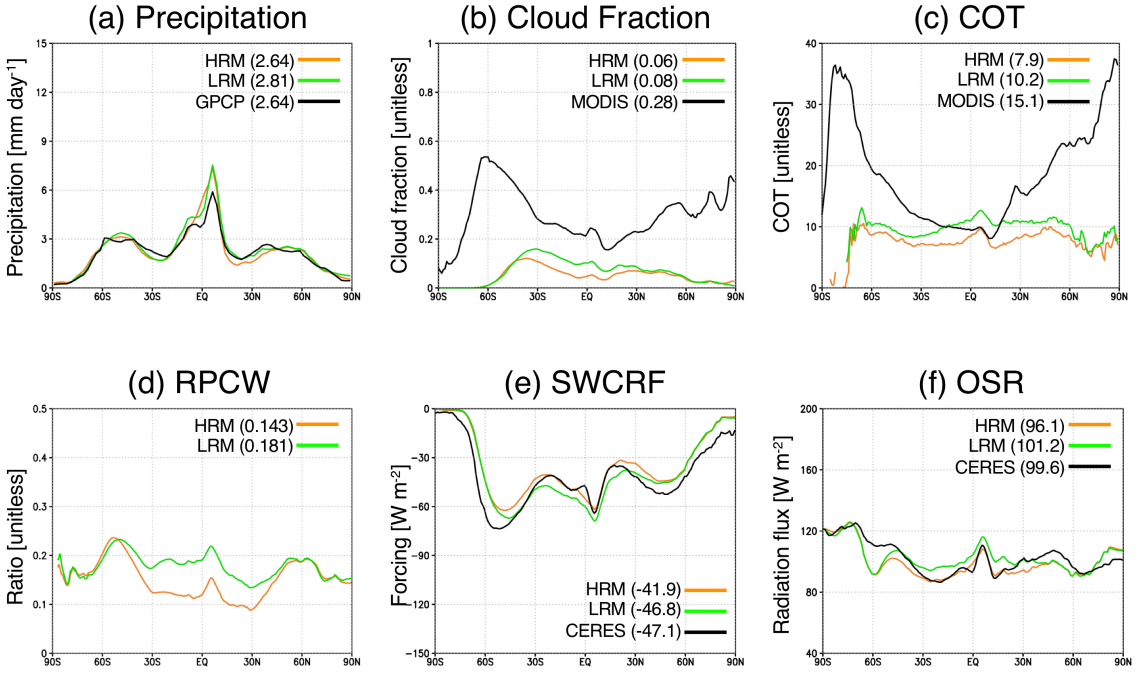

Figure 3: Zonal distributions of the annual averages of the (a) precipitation, (b) cloud fraction (CF) for water-phase clouds, (c) cloud optical thickness (COT) for water-phase clouds, (d) ratio of precipitation to total cloud water (RPCW) at 2-km height, (e) short-wave cloud radiative forcing (SWCRF) and (f) outgoing shortwave radiation flux (OSR) simulated by the HRM and LRM, reanalyzed by the GPCP only in (a), retrieved from the MODIS in (b) and (c) and estimated by the CERES in (e) and (f). The annual averages of these variables except for CF and COT are calculated by a 3-year integration, whereas those in CF and COT are calculated by a 1-year integration using 6-hourly instantaneous clouds at 12:00 (local time) to more exactly compare them with the observed MODIS/Terra at approximately 14:00 (local time). The numbers shown in the captions represent the global and annual averages for NICAM (HRM or LRM) and the reference data. The units are described in each panel.

https://doi.org/10.5194/gmd-2020-34
Preprint. Discussion started: 26 February 2020

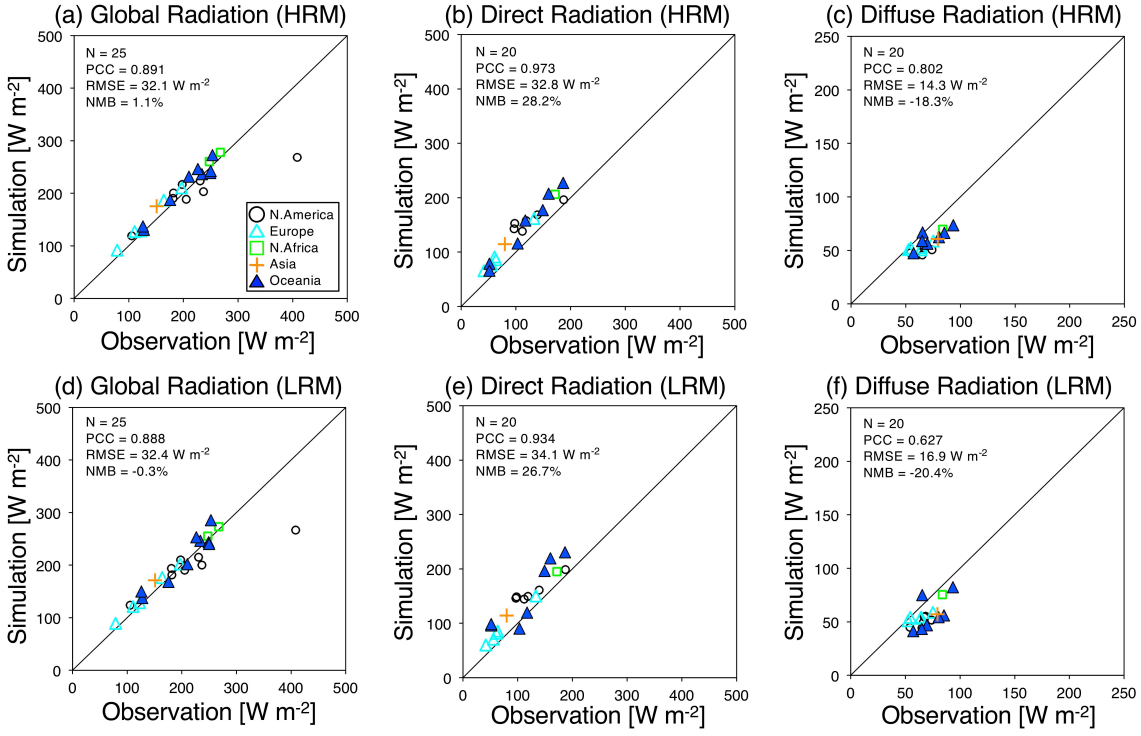

Figure 4: Scatterplots of the (a,d) global, (b,e) direct and (c,f) diffuse radiation fluxes between the BSRN measurements and NICAM simulations (HRM and LRM) for global annual averages. The different colors and marks reflect the sites in the different regions explained in panel (a). The numbers located in the upper-left corner in each panel represent the statistical metrics: the sampling number (N), PCC, RMSE and NMB. All units are in W m^{-2}.

https://doi.org/10.5194/gmd-2020-34
Preprint. Discussion started: 26 February 2020

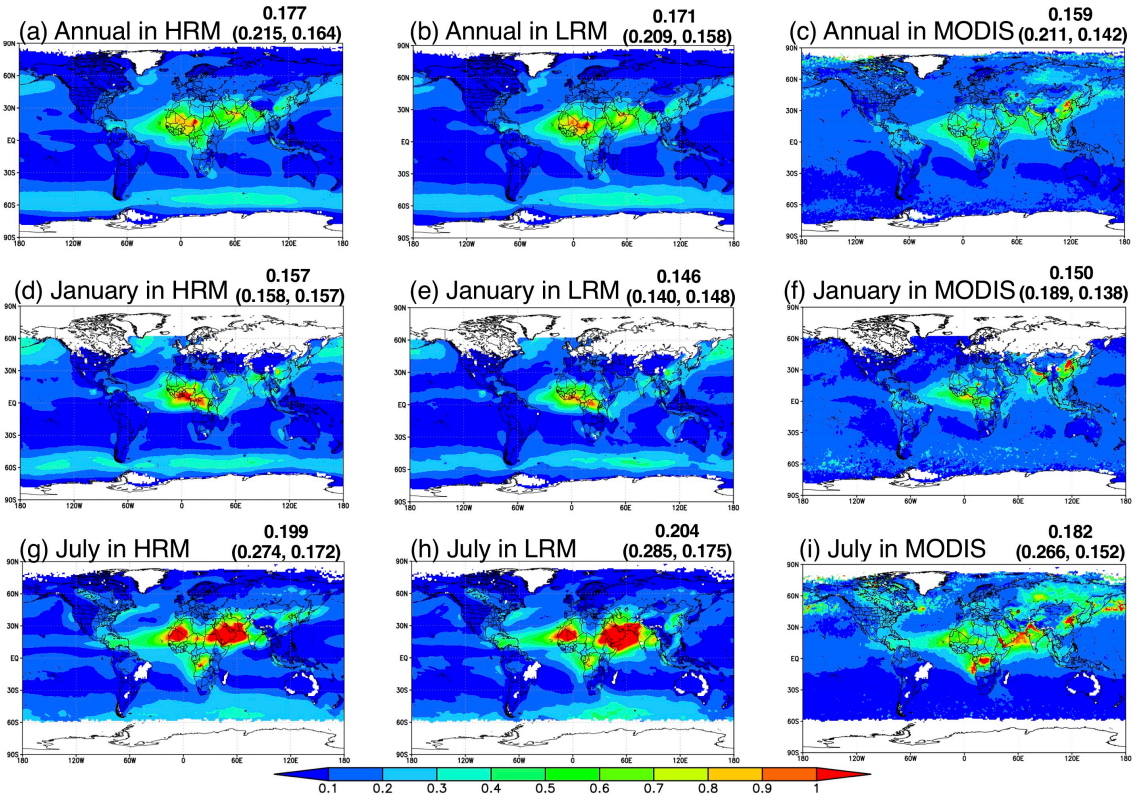

Figure 5: Same as Figure 2 but for the AOT. The reference data are the observations by MODIS/Terra. The model results in both the HRM and the LRM are horizontally interpolated onto the MODIS grids (1°×1°). The numbers shown in the upper-right corner in each panel represent the annual and semiglobal averages (60°S-60°N); those in brackets represent the global land and ocean averages.

https://doi.org/10.5194/gmd-2020-34
Preprint. Discussion started: 26 February 2020

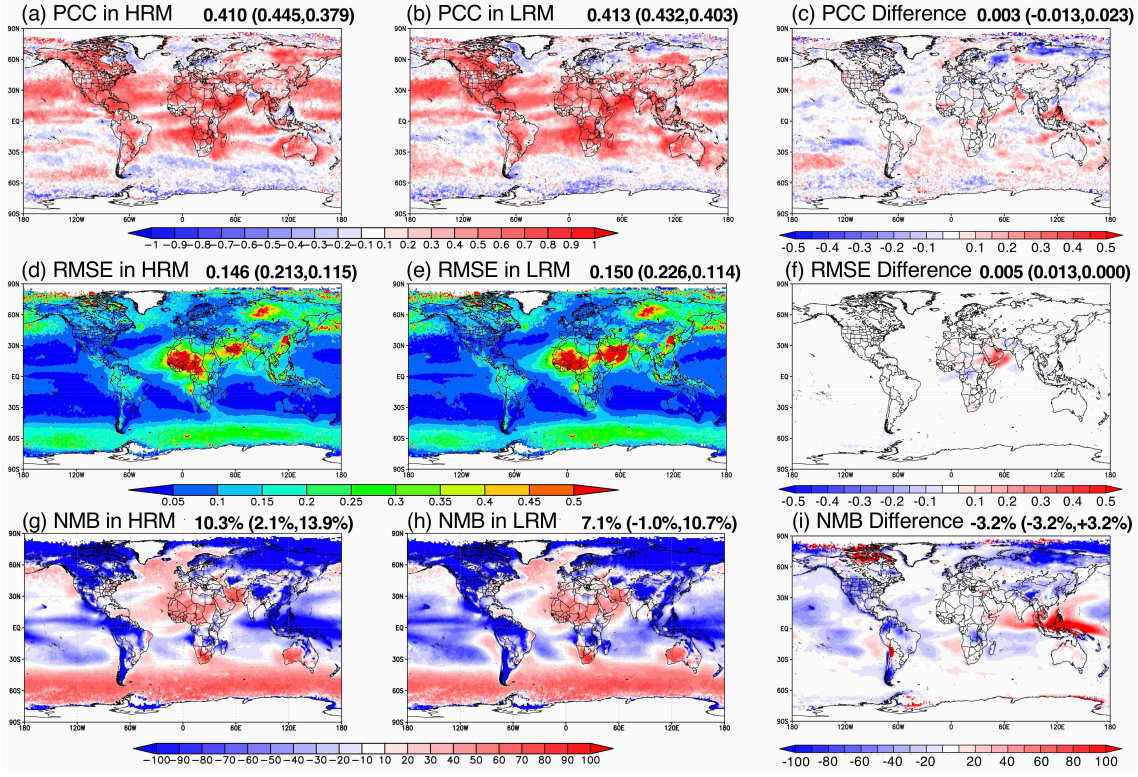

Figure 6: Global distributions of the statistical metrics, i.e., the (a,b) PCC, (d,e) RMSE and (g,h) NMB, between the NICAM (HRM and LRM) simulations and MODIS retrievals for the annual averages and (c,f,i) the differences in these metrics between the HRM and LRM, i.e., LRM minus HRM. These metrics are calculated using data representing 12-monthly averages over three years in each grid (1°×1°). The numbers shown in the upper-right corner without the brackets in each panel represent semiglobal averages (60°S-60°N) without undefined grids in MODIS using the 12-monthly averages; those in brackets represent the global land and ocean averages.

https://doi.org/10.5194/gmd-2020-34
Preprint. Discussion started: 26 February 2020

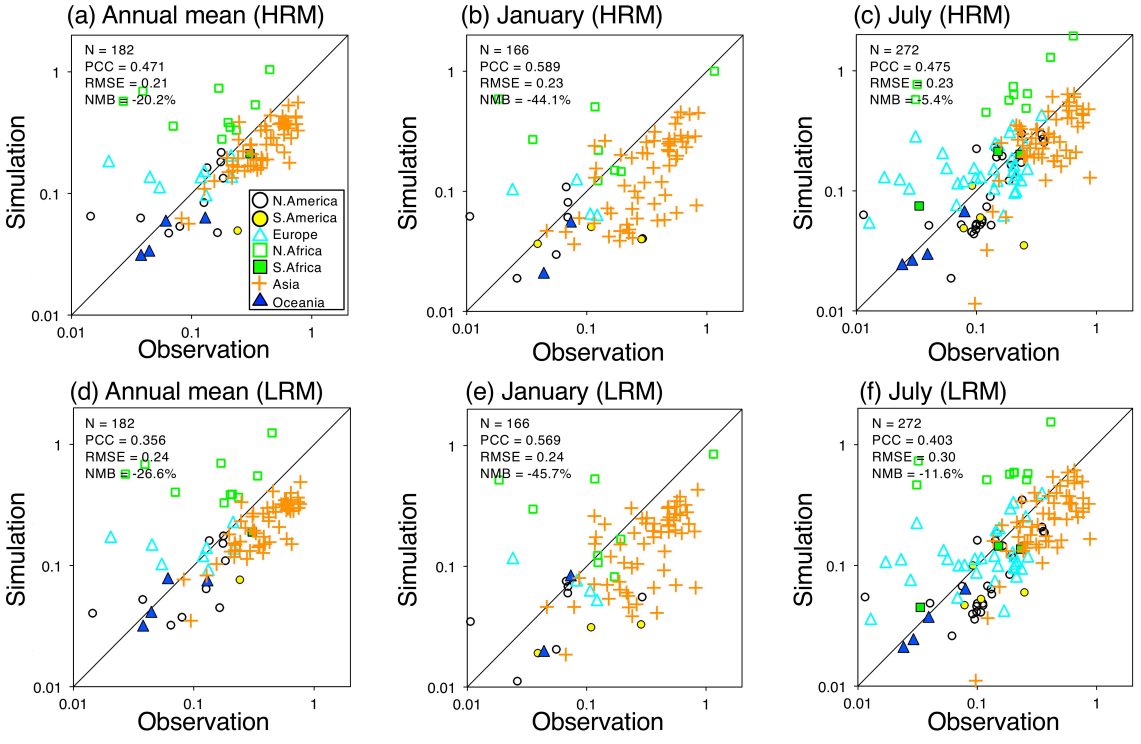

Figure 7: Scatterplot of the AOT at a wavelength of 500 nm between satellite measurements (AERONET, SKYNET, CARSNET) and the NICAM (HRM and LRM) simulations for the annual, January and July averages. The different colors and marks reflect the sites in the different regions explained in panel (a). The numbers located in the upper-left corner in each panel represent the statistical metrics: N, PCC, RMSE and NMB. The sites used for the comparison are shown in Figure 1.

https://doi.org/10.5194/gmd-2020-34
Preprint. Discussion started: 26 February 2020

Geoscientific Model Development Discussions
Open Access
EGU

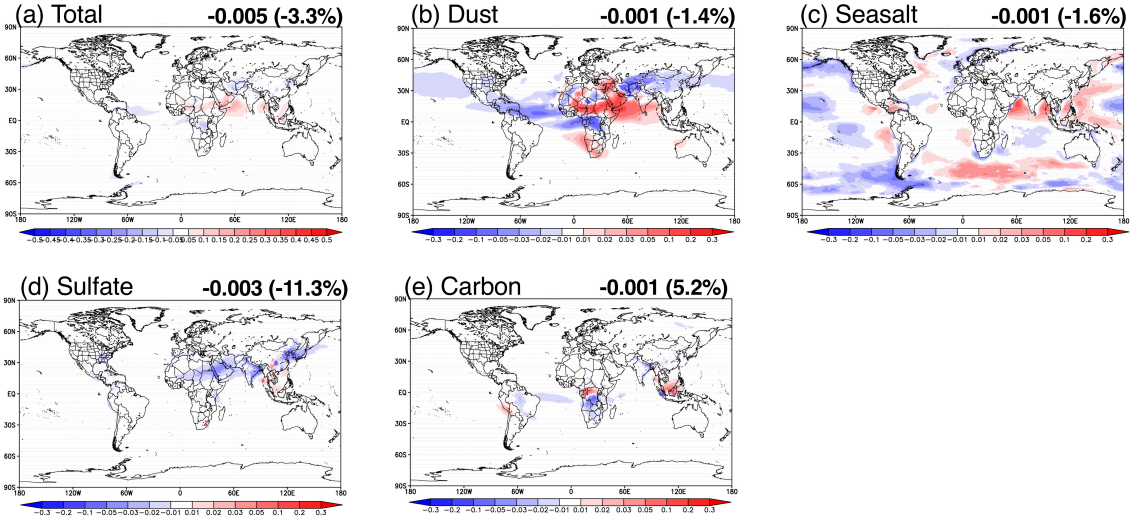

Figure 8: Global distributions of the differences in the (a) total AOT and (b,c,d,e) AOT components (dust, sea salt, sulfate and total carbonaceous aerosols, respectively) between the HRM and LRM (LRM minus HRM) for the annual averages. The numbers shown in upper-right corner in each panel represent the annual and global averages of the difference, and the numbers in brackets represent the annual and global averages of the relative difference in units of %.

https://doi.org/10.5194/gmd-2020-34
Preprint. Discussion started: 26 February 2020

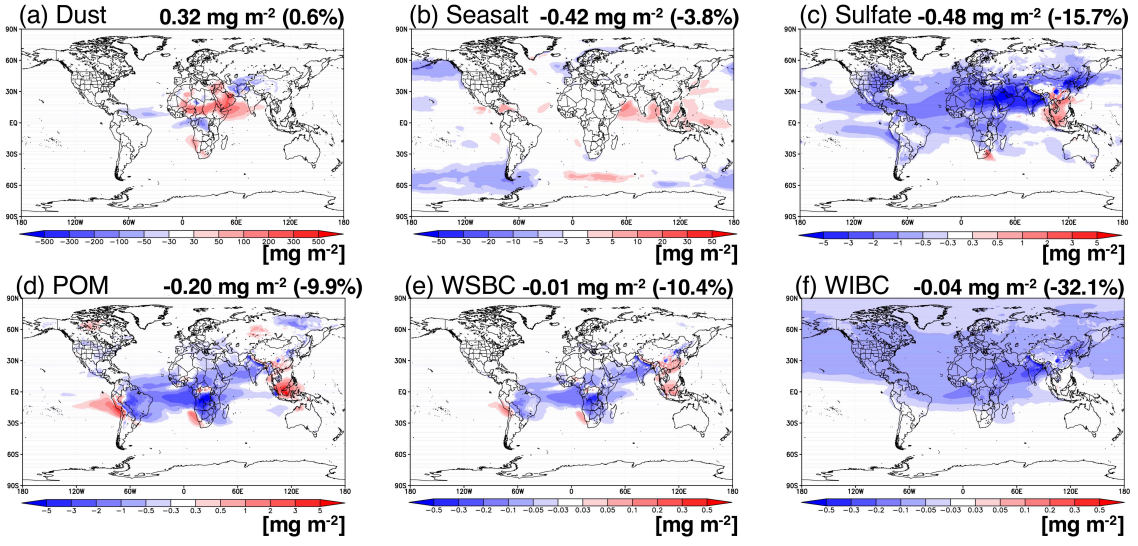

Figure 9: Global distribution of the differences in the mass loadings of (a) dust, (b) sea salt, (c) sulfate, (d) POM, (e) WSBC and (f) WIBC between the HRM and LRM (LRM minus HRM) for the annual averages. The numbers shown in the upper-right corner in each panel represent the annual and global averages of the difference in units of mg m^{-2}, and the numbers in brackets represent the annual and global averages of the relative difference in units of %.

https://doi.org/10.5194/gmd-2020-34
Preprint. Discussion started: 26 February 2020

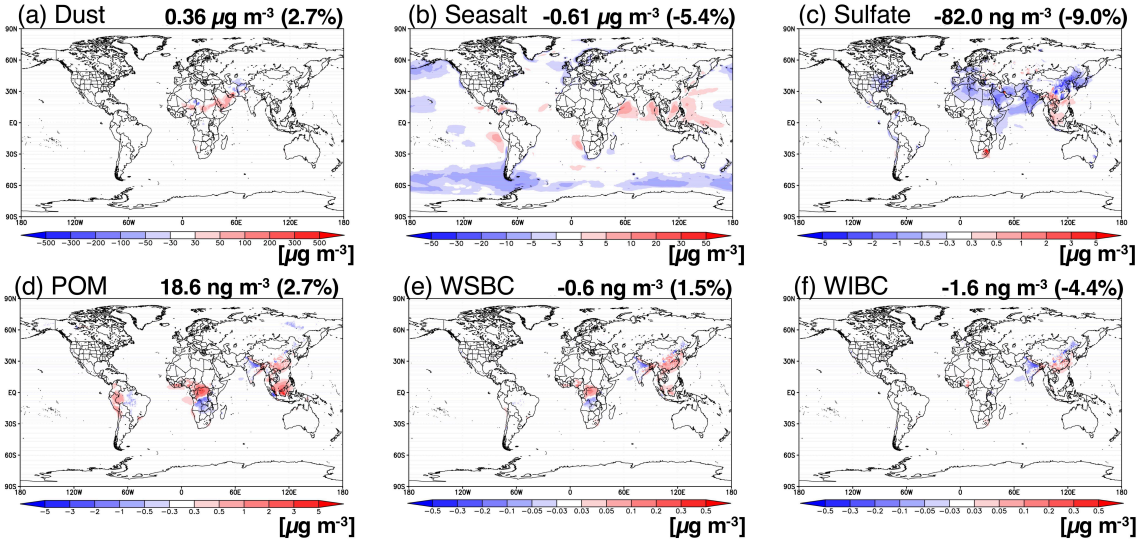

Figure 10: Same as Figure 9 but for the surface mass concentrations in units of μg m^{-3}.

https://doi.org/10.5194/gmd-2020-34
Preprint. Discussion started: 26 February 2020

Geoscientific Model Development Discussions

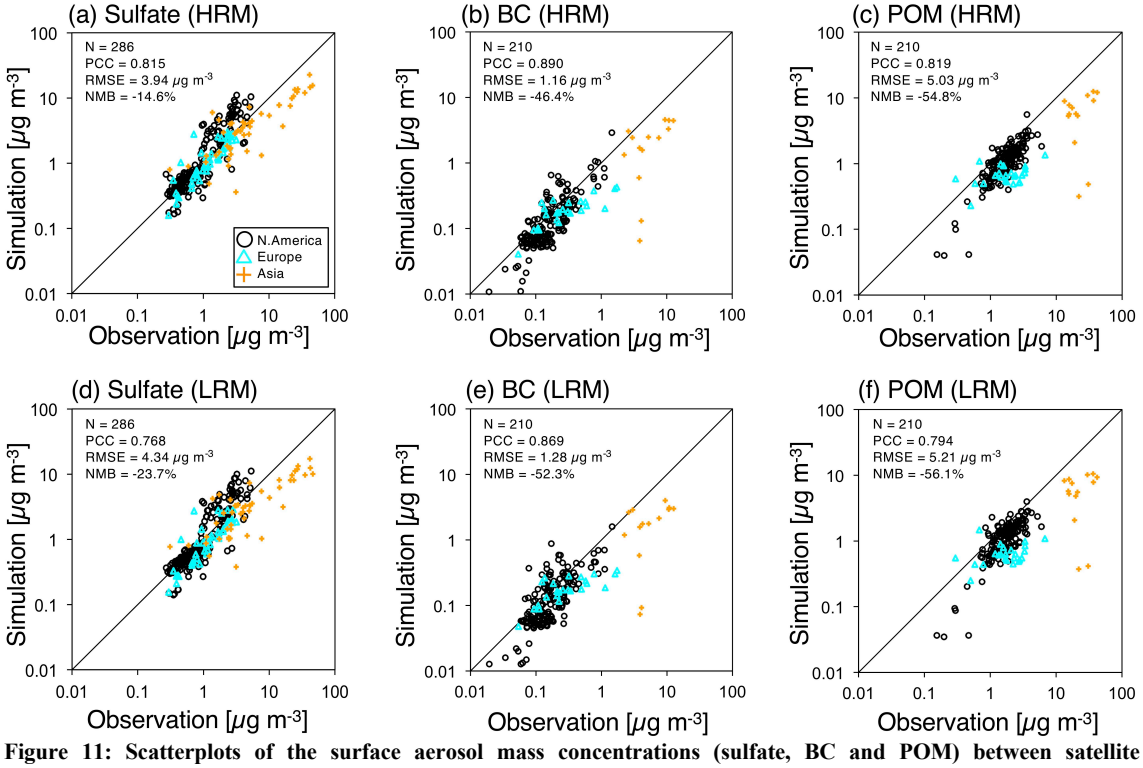

Figure 11: Scatterplots of the surface aerosol mass concentrations (sulfate, BC and POM) between satellite measurements (IMPROVE, EMEP, EANET and CAWNET) and the NICAM (HRM and LRM) simulations for the annual averages. All units are in μg m^{-3}. The different colors and marks reflect the sites in the different regions explained in panel (a). The numbers located in the upper-left corner in each panel represent the statistical metrics: N, PCC, RMSE and NMB. The sites employed for the comparison are shown in Figure 1.

https://doi.org/10.5194/gmd-2020-34
Preprint. Discussion started: 26 February 2020

Geoscientific Model Development Discussions

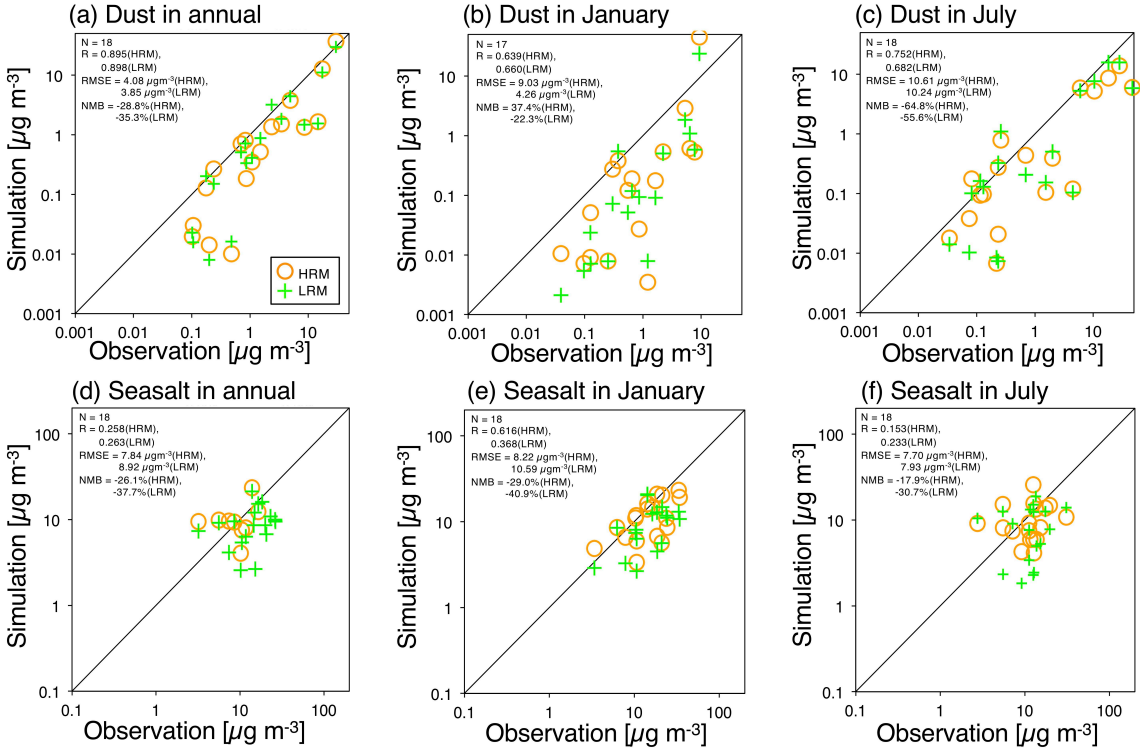

Figure 12: Scatterplots of the surface aerosol mass concentrations (dust and sea salt) between the measurements (the network managed by the University of Miami) and NICAM simulations (HRM in orange and LRM in green) for the annual, January and July averages. All units are in μg m^{-3}. The numbers located in the upper-left corner in each panel represent the statistical metrics: N, PCC, RMSE and NMB. The sites employed for the comparison are shown in Figure 1.

https://doi.org/10.5194/gmd-2020-34
Preprint. Discussion started: 26 February 2020

Geoscientific Model Development Discussions

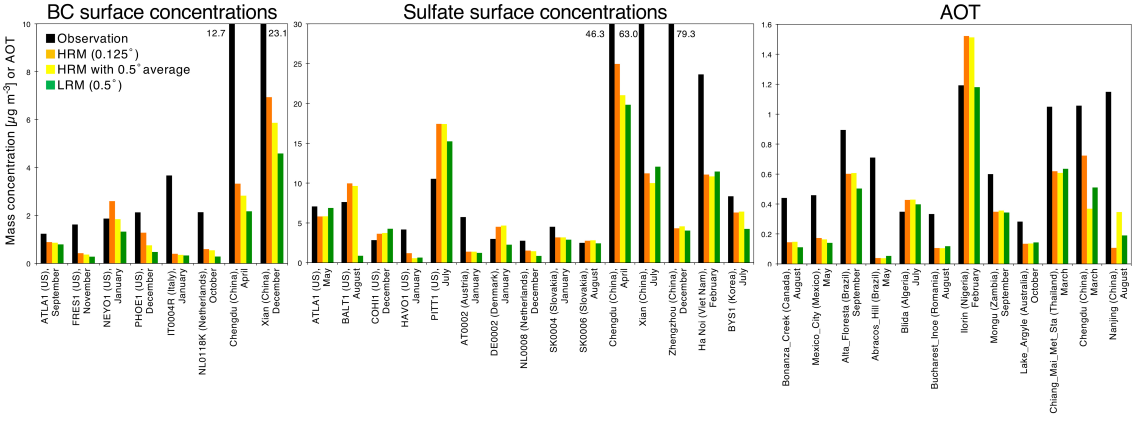

Figure 13: Multiple comparisons of the BC and sulfate surface mass concentrations (μg m^{-3}) and AOTs at the polluted sites using the HRM with the original grid of 0.125°×0.125°, the HRM with the interpolated grid of 0.5°×0.5° (denoted as 'HRM with 0.5° average'), the LRM with the original grid of 0.5°×0.5°, and the observations. The abscissa shows the selected sites, which were selected by choosing the highest values at the sites in each domain and month.

https://doi.org/10.5194/gmd-2020-34
Preprint. Discussion started: 26 February 2020

Geoscientific Model Development Discussions
Open Access
EGU

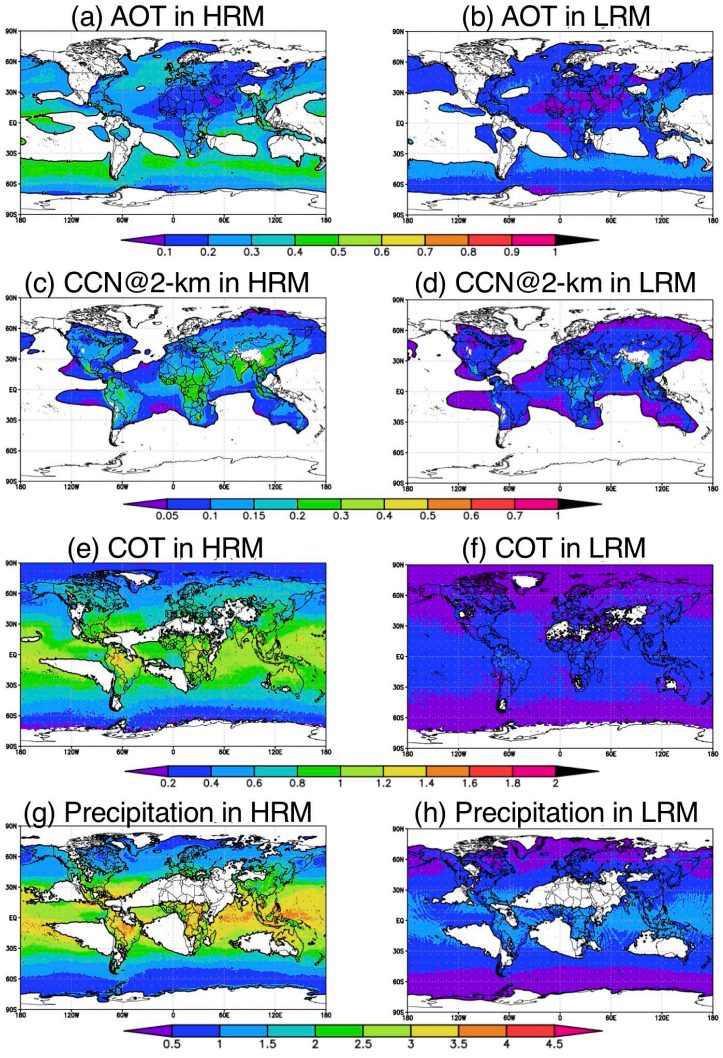

Figure 14: Global distributions of the ratio of the standard deviation to the average for the (a,b) AOT, (c,d) CCN at a height of approximately 2 km, (e,f) COT and (g,h) precipitation in 1°×1° grids using the 6-hourly output of both the HRM and the LRM for a 1-year integration period. All units are in %. The transparency represents lower absolute values of each parameter: AOTs of <0.1 in panels (a,b), CCN of <40 cm^{-3} in panels (c,d), COTs of <5 in panels (e,f), and precipitation fluxes of <1 mm day^{-1} in panels (g,h).

https://doi.org/10.5194/gmd-2020-34
Preprint. Discussion started: 26 February 2020

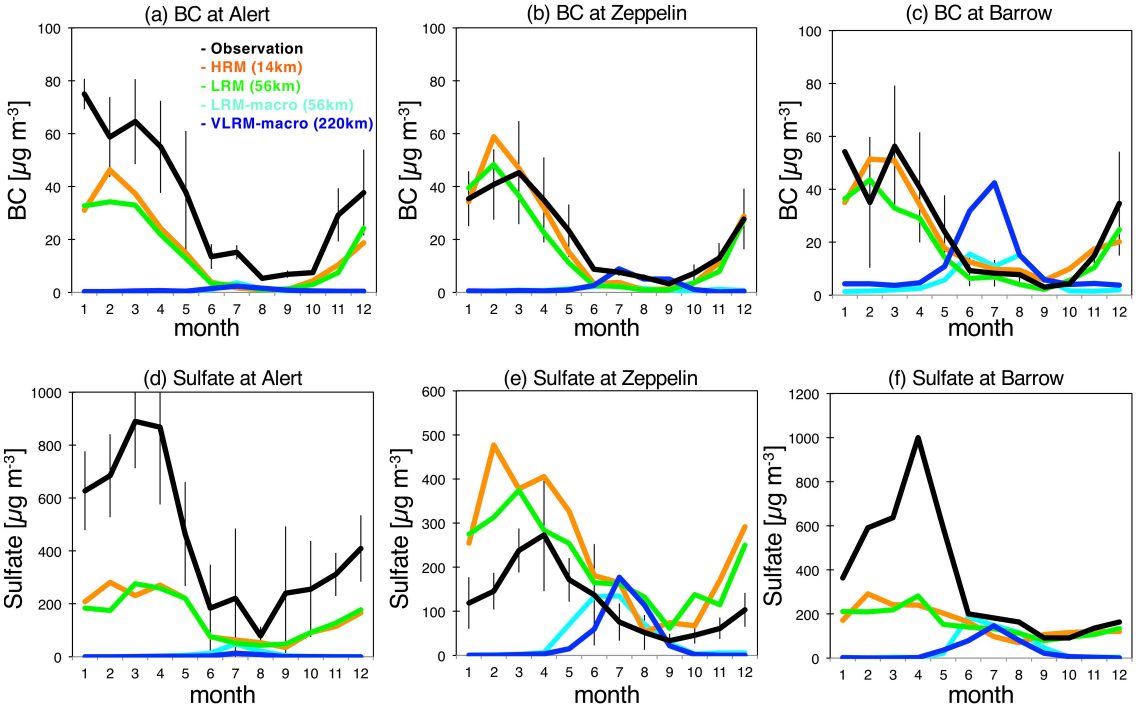

Figure 15: Monthly averages of BC and sulfate concentrations simulated by the HRM, LRM, LRM with a cloud macrophysics module (LRM-macro) and VLRM-macro (NICAM simulations using a horizontal grid spacing of 220 km with the cloud macrophysics module) at three Arctic sites: Alert (62.3°W, 82.5°N), Zeppelin (11.9°E, 78.9°N) and Barrow (157.0°W, 71.3°N). The BC is measured as the equivalent BC at 530 nm by a particle soot absorption photometer (PSAP) for 2007-2001 under the EMEP and WDCS databases (http://ebas.nilu.no). The sulfate concentrations are averaged at Alert for 2000-2006 by the Canadian Aerosol Baseline Measurement (CABM) program, at Zeppelin for 2005-2013 by EMEP, and at Barrow for 2008-2009 by Eckhardt et al. (2015).

https://doi.org/10.5194/gmd-2020-34
Preprint. Discussion started: 26 February 2020

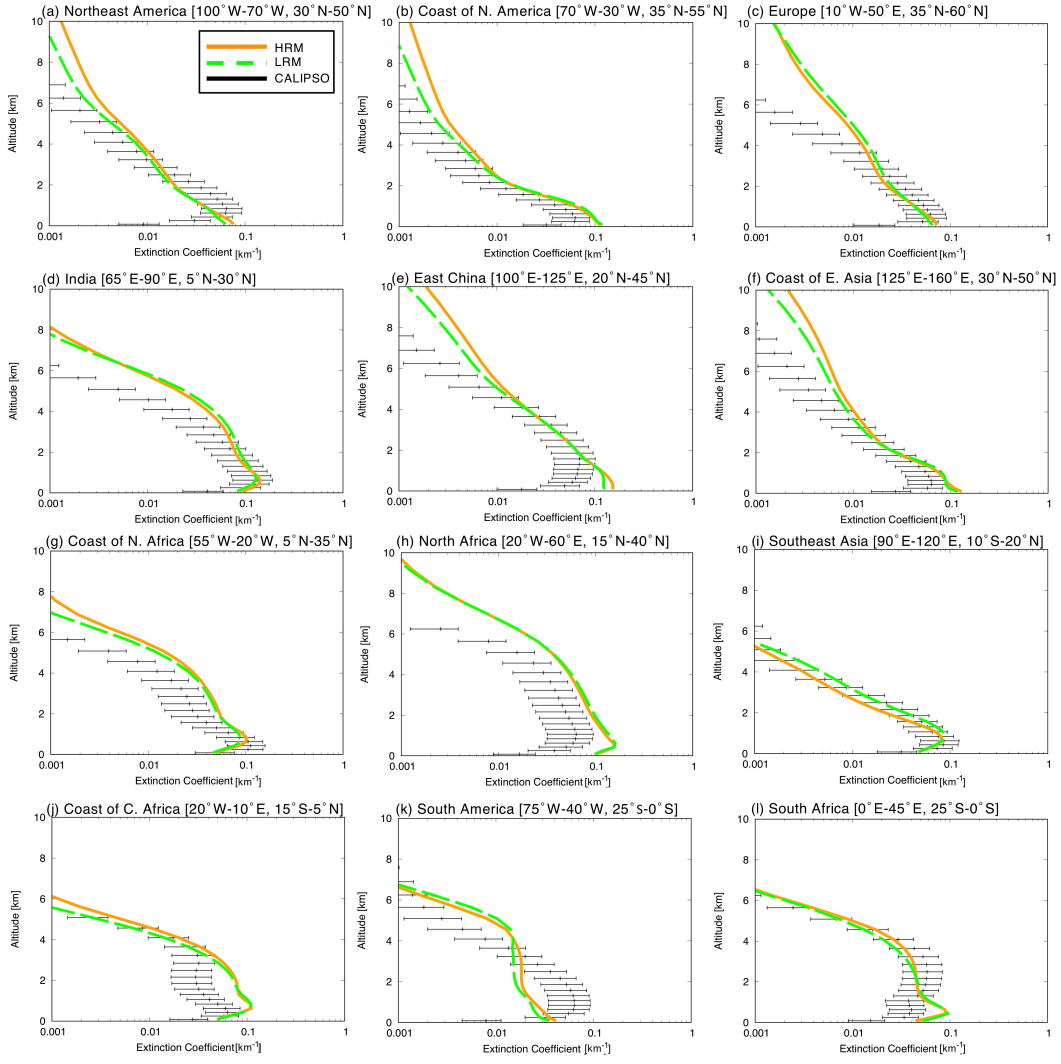

Figure 16: Vertical distributions of the annually averaged aerosol extinction coefficients from the NICAM simulations (HRM in orange and LRM in green) and from CALIOP/CALIPSO observations (black) in 12 different regions. The definition of the region is based on Koffi et al. (2016), except for panels (i) Southeast Asia and (j) the coast of Central Africa. The CALIOP-retrieved results are shown as bars, which are the standard deviation of the results from a 3-year integration period.

https://doi.org/10.5194/gmd-2020-34
Preprint. Discussion started: 26 February 2020

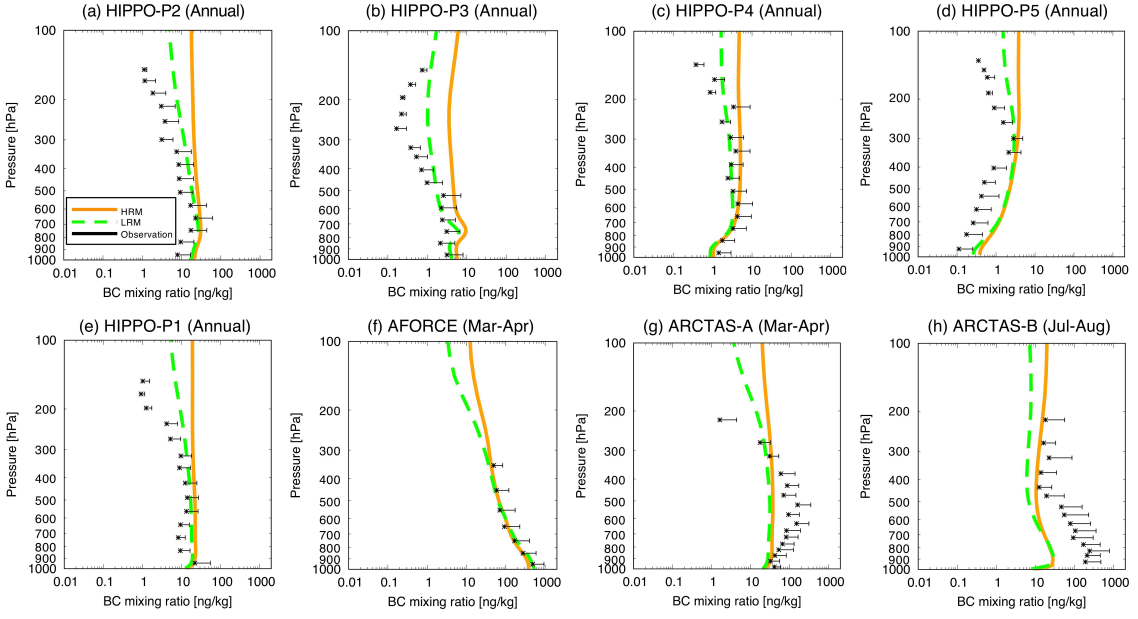

Figure 17: Vertical distribution of the BC mass concentrations from the NICAM simulations (HRM in orange and LRM in green) and from flight campaign measurements (the groups by NOAA and the University of Tokyo) in various regions and seasons. The definitions of the target domain and period in each panel are as follows: (a) 20°N-60°N, 160°E-150°W, (b) 20°S-20°N, 160°E-150°W, (c) 60°S-20°S, 160°E-150°W, (b) 60°S-80°S, 160°E-150°W, and (e) 60°N-90°N, 160°E-150°W in annual averages, (f) 32°N-37°N, 122°E-126°E in March and 26°N-32°N, 126°E-132°E in April, (g) 60°N-80°N, 165°W-70°W in March-April and (h) 45°N-87°N, 135°W-45°W in July-August. The abscissa shows the mass concentration in units of μg m^{-3}, and the ordinate shows the air pressure in units of hPa.

https://doi.org/10.5194/gmd-2020-34
Preprint. Discussion started: 26 February 2020

Geoscientific Model Development Discussions
Open Access
EGU

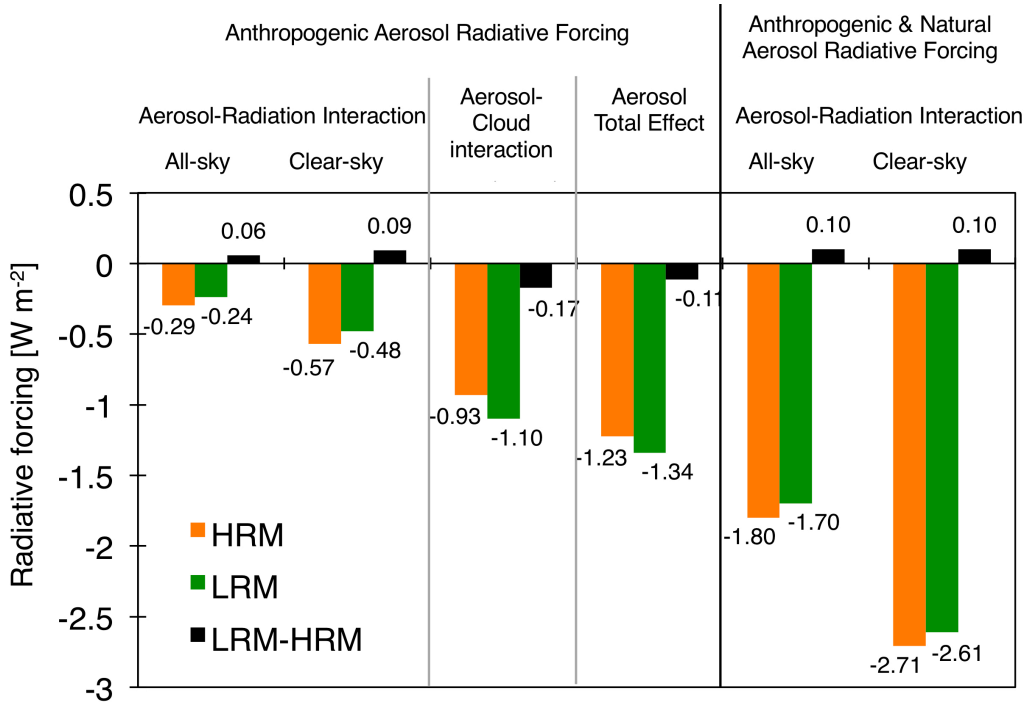

Figure 18: Annual global average ARFs for both ARIs and ACIs against anthropogenic and total aerosols, i.e., anthropogenic and natural sources, under all-sky and clear-sky conditions at the TOA using the HRM (orange), the LRM (green) and the difference (LRM minus HRM in black). All units are in Wm^{-2}.

https://doi.org/10.5194/gmd-2020-34
Preprint. Discussion started: 26 February 2020

Geoscientific Model Development Discussions
Open Access
EGU

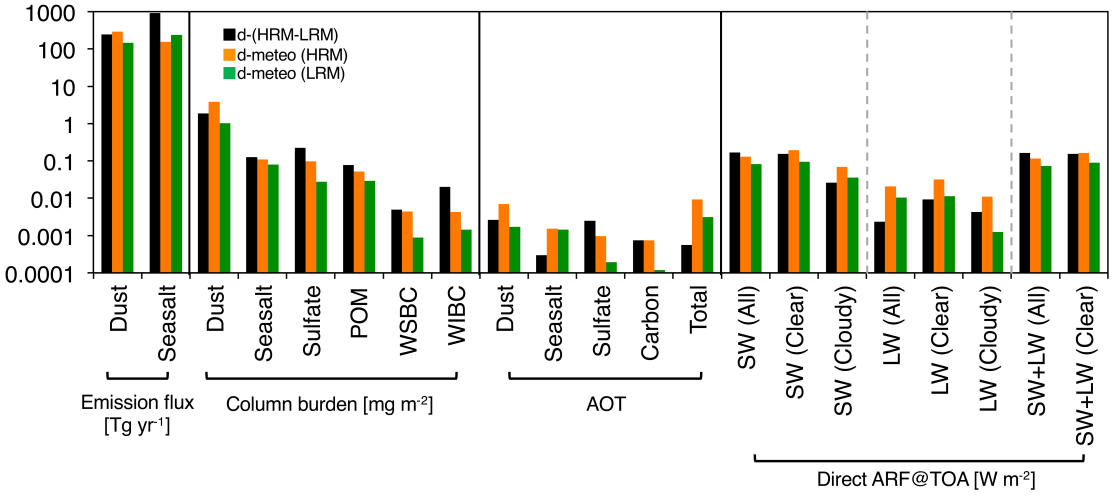

Figure 19: Variabilities of the emission fluxes (for dust and sea salt), column burdens (for dust, sea salt, sulfate, OC, WSBC and WIBC), AOTs (for dust, sea salt, sulfate, carbon and total amount) and direct ARF at the TOA (shortwave (SW), longwave (LW) and total (SW plus LW) under all-sky, clear-sky and cloudy-sky conditions) by perturbing the meteorological fields, i.e., considering the variabilities for the 3-year integration of the NICAM. The results are shown in three panels: 'd-(HRM-LRM)' represents the difference between the HRM and LRM, 'd-meteo (HRM)' represents the difference among the 3 years of integration results in the HRM, and 'd-meteo (LRM)' represents the difference among the 3 years of integration results in the LRM.